Parameter estimation for space-based gravitational wave detectors with ringdown signals

Chunyu Zhang (张春雨)⬤,[†] Yungui Gong (龚云贵)⬤,[*] and Chao Zhang (张超)⬤[‡]

School of Physics, Huazhong University of Science and Technology, Wuhan, Hubei 430074, China

Unlike ground-based gravitational wave detectors, space-based gravitational wave detectors can detect the ringdown signals from massive black hole mergers with large signal-to-noise ratios, help to localize sources and extract their parameters. To reduce the computation time in the Fisher information matrix analysis, we derive the analytical formulas of frequency-domain ringdown signals for both heliocentric and geocentric detectors by considering the effects of the harmonic phases, the rotation period of the geocentric detector, and the detector's arm length. We explore median errors of the parameter estimation and source localization with ringdown signals from binaries with different masses and different redshifts. Using a binary source with the total mass $M = 10^7 \, M_\odot$ at the redshift $z = 1$, we analyze the dependence of these errors on the sky position. We find that the network of space-based gravitational wave detectors can significantly improve the source localization at the ringdown stage. The results of the Fisher matrix approximation are also checked by Bayesian inference method.

I. INTRODUCTION

The detection of gravitational waves (GWs) by the Laser Interferometer Gravitational-Wave Observatory (LIGO) Scientific Collaboration and the Virgo Collaboration not only announced the dawn of a new era of multimessenger astronomy, but also opened a new window to probe the nature of gravity and spacetime in the nonlinear and strong field regimes [1–13]. GWs from compact binary coalescences consist of inspiral, merger, and ringdown phases, with increasing frequency. The inspiral waves, at the stage of orbiting until the innermost stable orbit, can be analyzed by the post-Newtonian theory, black hole (BH) perturbation theory, etc. At the early inspiral stage, the emitted GWs can be regarded as monochromatic waves due to the slow orbital decay. The merger waveform which is not well modeled at present, is the research topic in numerical relativity. The ringdown signal originating from the distorted final BH, comprises a superposition of quasinormal modes (QNMs). The frequency of each mode is a complex number, the real part is the oscillation frequency, and the imaginary part is the inverse of the damping time. These frequencies are determined by the mass M and angular momentum J of the final BH, and the amplitude and phase of each mode are determined by the specific process when the final BH forms.

Ground-based GW detectors, such as Advanced LIGO [14,15], Advanced Virgo [16] and Kamioka Gravitational Wave Detector (KAGRA) [17,18], operate in the $10 - 10^4$ Hz frequency band. In this frequency band, the detected events are stellar-mass binary mergers, the ringdown signal is not loud enough to probe the physics behind it. The proposed space-based GW detectors such as Laser Interferometer Space Antenna (LISA) [19,20], TianQin [21], and Taiji [22] probe GWs in the millihertz frequency band, while Deci-hertz Interferometer Gravitational Wave Observatory (DECIGO) [23] operates in the 0.1 to 10 Hz frequency band. Thus, space-based GW detectors can detect ringdown signals from massive BH binary mergers with large signal-to-noise ratios (SNRs), and the detected ringdown signals can be used to probe the nature of BHs, localize sources and estimate their parameters, etc. In particular, the sky localization of the source is one of the important scientific objectives for GW observations because accurate information about the source localization is necessary for the follow-up observations of electromagnetic counterparts and the statistical identification of the host galaxy if no counterpart is present. Therefore, cosmological applications such as studying the problem of Hubble tension [24] using GWs as standard sirens [25,26] depend critically on the capability of locating the source accurately.

In general, higher multipoles and higher harmonics are subdominant in the inspiral phase, so usually the parameter estimation for space-based GW detectors was analyzed with Fisher information matrix (FIM) method by

─────────
[*]Corresponding author.
yggong@hust.edu.cn
[†]chunyuzhang@hust.edu.cn
[‡]chao_zhang@hust.edu.cn

considering the (2, 2) mode only [27–53]. The parameter estimation as function of time left before merger was also discussed in [53]. Higher multipoles and higher harmonics of GWs have characteristic structure in the gravitational waveforms, and they have different dependence on the source's parameters such as the inclination, the mass ratio and spins, so they can be used to break some of the degeneracies between the parameters and improve the parameter estimation accuracy [54–60]. Furthermore, higher harmonics can break the degeneracy between the polarization and the coalescence phase [61]. Because the contribution of higher multipoles to the radiated energy increases with the mass ratio [62,63], the estimations of the mass ratio and the effective spin are improved with higher harmonics for the GW170729 event [64]. For heavier binaries with $M \gtrsim 10^7 \, M_\odot$, higher harmonics of inspiral can improve the angular resolution of LISA by a factor of ~ 100 [65–68]. If the total mass of a binary is very large, then the inspiral waves are out of the frequency band of space-based GW detectors and the ringdown waves with higher harmonics become dominant because they have higher frequencies [69–71]. For ringdown GWs, ignoring the source location, the capability of TianQin to test the no-hair theorem of general relativity was studied [72]. With higher harmonics of the ringdown signals from binaries with the total mass $M \geq 10^6 \, M_\odot$, employing the error propagation method in FIM and ignoring the influences of the arm length and harmonic phases, the parameter estimation and source localization of LISA were studied in Ref. [73]. Compared with Bayesian inference method, the FIM method provides poor estimations for the extrinsic parameters such as sky location, luminosity distance and inclination angle and we cannot make strong statements about parameter estimation with massive BH binaries using the FIM method [74–76]. It was shown that higher harmonics can break degeneracies between parameters and considerably improve the source localization of massive BH binaries with LISA by using Bayesian parameter estimation [76]. With Bayesian inference method, varied correlations between the total masses and mass ratios and the ability of sky localization of the source with LISA were discussed by analyzing seven test massive BH binaries using the PhenomHM waveform with higher harmonics and aligned spins [77].

Note that to perform parameter estimation, we need to identify the presence of a signal first. In reality, data gaps, glitches, nonstationary and non-Guassian noises, orbital evolution, unequal arms and superposed signals of different types, all increase the complexity of data analysis [75,76,78–86]. To cancel the large laser frequency noise in an unequal arm interferometer detector, Time-delay interferometry was proposed in [84,85]. Dey *et al.* found that the effect of data gaps due to regular maintenance of the spacecraft on the detection and parameter estimation of massive BH binaries with LISA is

negligible [86]. In this paper, we leave aside these problems and focus on the inference of BH parameters.

The purpose of this paper is to derive analytical frequency-domain detector signals at the ringdown stage, and use them to make parameter estimation. The paper is organized as follows. In Sec. II, we give the analytical formulas of frequency-domain ringdown signals for both heliocentric and geocentric detectors by considering the influences of the harmonic phases, the rotation period of the geocentric detector, and the detector's arm length. The integration formulas we used are presented in Appendix A. In Sec. III, we show the median errors of the parameters and the source localization with ringdown signals from binaries with different total masses and different redshifts. We also analyze the dependence of these errors on the sky position. Then we explore the localization capability of different detectors including the network of space-based GW detectors. In Sec. IV, we choose two binaries for parameter estimation with Bayesian inference method to check the FIM results. We conclude this paper in Sec. V. Throughout this paper we use units in which $G = c = 1$.

II. METHODOLOGY

A. Ringdown waves

Distorted BHs, such as the newly formed remnant after the coalescence of two BHs, are expected to emit characteristic radiation in the form of QNMs, called ringdown waves, with discrete frequencies. We usually use three indices (l, m, n) to label the QNMs, where $n = 0, 1, 2, \ldots$ is the overtone index, and $l = 2, 3, 4, \ldots$ and $m = 0, \pm 1, \ldots, \pm l$ are the harmonic indices. Compared to higher overtones with $n \geq 1$, the fundamental modes with $n = 0$ usually have much larger amplitudes and much longer damping times. Thus we only consider the fundamental modes with $n = 0$ and denote them as (ℓ, m). Due to the similar reason, and to avoid large numerical-relativity errors, we only use the four strongest modes $(\ell, m) = (2, 2), (3, 3), (2, 1), (4, 4)$,

$$h_+(t) = \frac{M_z}{d_L} \sum_{\ell,m} A_{\ell m} Y_+^{\ell m}(\iota) e^{-\frac{t}{\tau_{\ell m}}} \cos(\omega_{\ell m} t - \phi_{\ell m}),$$

$$h_\times(t) = -\frac{M_z}{d_L} \sum_{\ell,m} A_{\ell m} Y_\times^{\ell m}(\iota) e^{-\frac{t}{\tau_{\ell m}}} \sin(\omega_{\ell m} t - \phi_{\ell m}) \quad (1)$$

for $t > t_0$; and $h_{+,\times}(t) = 0$ for $t < t_0$. Here t_0 is the start time of the ringdown waves, M_z is the redshifted mass of the remnant, d_L is the luminosity distance to the source, $A_{\ell m}, \omega_{\ell m}, \tau_{\ell m}$ and $\phi_{\ell m}$ are the amplitude, oscillation frequency, damping time, and initial phase of the corresponding QNM respectively, and $\iota \in [0, \pi]$ is the inclination angle of the source.

The functions $Y_{+,\times}^{\ell m}(\iota)$ corresponding to the two ringdown polarizations can be found by summing over modes with positive and negative m:

$$Y_+^{\ell m}(\iota) \equiv \,_{-2}Y^{\ell m}(\iota, 0) + (-1)^\ell \,_{-2}Y^{\ell -m}(\iota, 0),$$
$$Y_\times^{\ell m}(\iota) \equiv \,_{-2}Y^{\ell m}(\iota, 0) - (-1)^\ell \,_{-2}Y^{\ell -m}(\iota, 0). \quad (2)$$

For example,

$$Y_+^{22}(\iota) = \frac{1}{2}\sqrt{\frac{5}{\pi}}\frac{1 + (\cos\iota)^2}{2},$$

$$Y_\times^{22}(\iota) = \frac{1}{2}\sqrt{\frac{5}{\pi}}\cos\iota,$$

$$Y_+^{21}(\iota) = \sqrt{\frac{5}{4\pi}}\sin\iota,$$

$$Y_\times^{21}(\iota) = \sqrt{\frac{5}{4\pi}}\cos\iota\sin\iota,$$

$$Y_+^{33}(\iota) = -\sqrt{\frac{21}{8\pi}}\frac{(1 + \cos^2\iota)}{2}\sin\iota,$$

$$Y_\times^{33}(\iota) = -\sqrt{\frac{21}{8\pi}}\cos\iota\sin\iota,$$

$$Y_+^{44}(\iota) = \sqrt{\frac{63}{16\pi}}\frac{(1 + \cos^2\iota)}{2}\sin^2\iota,$$

$$Y_\times^{44}(\iota) = \sqrt{\frac{63}{16\pi}}\cos\iota\sin^2\iota. \quad (3)$$

The fitting formulas of $\omega_{\ell m}$ and $\tau_{\ell m}$ are given as [71]

$$\omega_{\ell m} = \frac{f_1 + f_2(1 - j)^{f_3}}{M_z},$$

$$\tau_{\ell m} = \frac{2(q_1 + q_2(1 - j)^{q_3})}{\omega_{\ell m}}, \quad (4)$$

where the coefficients are listed in Table I, and j is the spin of the remnant. For mergers of nonspinning BHs, j is only a function of the mass ratio $q = M_1/M_2$ ($q \geq 1$) which can be approximated as $j(q) = \eta(2\sqrt{3} - 3.5171\eta + 2.5763\eta^2)$ [87], and the fitting formulas of $A_{\ell m}$ are given in Refs. [59,60]. Here $\eta = q/(1 + q)^2$ is the symmetric mass ratio.

In this paper, we take $q = 2$. In fact, for different q ($1 < q \leq 10$), the difference of the results for the parameter estimation and source localization is mostly within one order of magnitude as shown in Fig. 1.

TABLE I.   The coefficients [71] in Eq. (4).

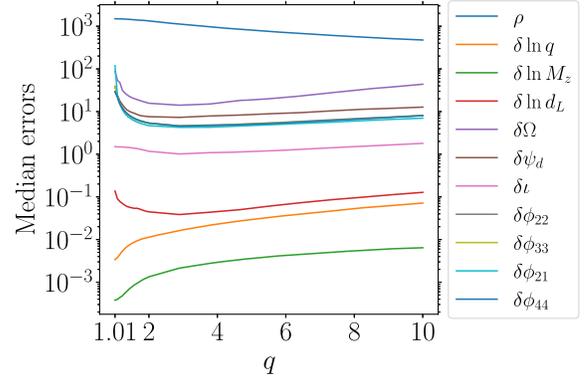| (ℓ, m)	f_1	f_2	f_3	q_1	q_2	q_3
(2, 2)	1.5251	−1.1568	0.1292	0.7000	1.4187	−0.4990
(3, 3)	1.8956	−1.3043	0.1818	0.9000	2.3430	−0.4810
(2, 1)	0.6000	−0.2339	0.4175	−0.3000	2.3561	−0.2277
(4, 4)	2.3000	−1.5056	0.2244	1.1929	3.1191	−0.4825

FIG. 1.   The effect of the mass ratio on the median errors of the parameters and the source localization with TianQin for the binary with the total mass $M = 10^6\, M_\odot$ at the redshift $z = 1$.

B. Polarization tensors

In the heliocentric coordinate $\{\hat{i}, \hat{j}, \hat{k}\}$, the GW coordinate basis vectors $\{\hat{m}, \hat{n}, \hat{o}\}$ are determined by the source location (θ_s, ϕ_s) and the polarization angle ψ_s as

$$\{\hat{m}, \hat{n}, \hat{o}\} = \{\hat{i}, \hat{j}, \hat{k}\} \times R_z(\phi_s - \pi)R_y(\pi - \theta_s)R_z(\psi_s), \quad (5)$$

where $\hat{o}$ is the propagating direction of GWs, and R_x, R_y, and R_z are Euler rotation matrices given by Eq. (B1).

In general relativity, there are two polarizations $A = +, \times$. With the help of polarization tensors e_{ij}^A,

$$e_{ij}^+ = \hat{m}_i\hat{m}_j - \hat{n}_i\hat{n}_j, \qquad e_{ij}^\times = \hat{m}_i\hat{n}_j + \hat{n}_i\hat{m}_j, \quad (6)$$

we can decompose GWs into two polarizations $h_{ij} = \sum_{A=+,\times} h_A e_{ij}^A$.

C. The detector signal

To use FIM to estimate parameters, we need the frequency-domain signal $s(f)$ in the detector. An analytical expression for $s(f)$ will help to speed up the computation and improve the precision. In Appendix A, we present the analytical formulas used in this paper.

At the ringdown stage, the damping time of GWs is normally within one day. Since space-based GW detectors take one year to orbit around the Sun, we treat the Doppler shift $\exp[-2\pi f\hat{o} \cdot \vec{r}_0/c]$, where $\vec{r}_0$ is the position of the center of mass of the detector in the heliocentric coordinate, as a constant at the ringdown stage. For convenience, we work in the detector coordinate as shown in Fig. 2. Although we put the detector in the x-y plane, it is straightforward to obtain the direction that the detector plane points to in the heliocentric coordinate. In the heliocentric coordinate, if the heliocentric detector (such as LISA and Taiji) is at $(\theta_s, \phi_s) = (\pi/2, \phi_0)$, then the normal vector of its detector plane will point to $(\theta_s, \phi_s) = (\pi/3, \phi_0 + \pi)$.
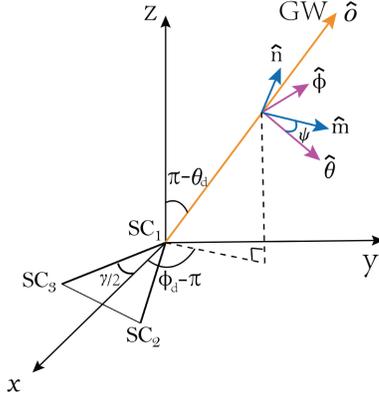
FIG. 2. The detector coordinate and the configuration of the detector with the opening angle $\gamma = \pi/3$.

In the detector coordinate, the polarization tensors are given by

$$e_{ij}^+ = \hat{m}_i\hat{m}_j - \hat{n}_i\hat{n}_j, \qquad e_{ij}^\times = \hat{m}_i\hat{n}_j + \hat{n}_i\hat{m}_j,$$

$$\{\hat{m}, \hat{n}, \hat{o}\} = R_z(\phi_d - \pi)R_y(\pi - \theta_d)R_z(\psi_d), \qquad (7)$$

where $(\theta_d, \phi_d, \psi_d)$ are source parameters in the detector coordinate, which are determined by $(\theta_s, \phi_s, \psi_s)$ through Eqs. (B1)–(B5).

The configurations of space-based GW detectors are generally equilateral triangles. We can model every detector of this kind as a combination of two independent LIGO-like detectors ("I" and "II") with the opening angle $\gamma = \pi/3$. Thus the signal in the detector II for a source at (θ_d, ϕ_d) is equivalent to the signal in the detector I for the same source but at $(\theta_d, \phi_d - 2\pi/3)$.

1. Geocentric detectors

Geocentric detectors orbit the Earth and further rotate around the Sun together with the Earth. We take TianQin as an example, whose detector plane faces to the source RX J0806.3 + 1527 at $(\theta_{tq} = 94.7°, \phi_{tq} = 120.5°)$ [88–92].

In the case of $10^5 M_\odot \leq M_z \leq 10^7 M_\odot$, the damping time of the ringdown signals is within 10 minutes. Thus we ignore the rotation of TianQin in this case. The frequency-domain detector signal is

$$s(f) = \sum_{A=+,\times}[D_u^A\mathcal{T}(f, \hat{u} \cdot \hat{o}) - D_v^A\mathcal{T}(f, \hat{v} \cdot \hat{o})]h_A(f), \quad (8)$$

where

$$D_u^A = \frac{1}{2}\hat{u}^i\hat{u}^j e_{ij}^A, \qquad D_v^A = \frac{1}{2}\hat{v}^i\hat{v}^j e_{ij}^A, \qquad (9)$$

the unit vectors of the detector's two arms are

$$\hat{u} = \left[\cos\left(\frac{\gamma}{2}\right), -\sin\left(\frac{\gamma}{2}\right), 0\right],$$

$$\hat{v} = \left[\cos\left(\frac{\gamma}{2}\right), \sin\left(\frac{\gamma}{2}\right), 0\right], \qquad (10)$$

and e_{ij}^A is the polarization tensor, given by Eq. (7). Combining Eqs. (7) and (10), we get

$$D_u^+ = \frac{1}{4}[(1 + \cos^2\theta_d)\cos(2\phi_d + \gamma) - \sin^2\theta_d]\cos(2\psi_d)$$
$$+ \frac{1}{2}\cos\theta_d\sin(2\phi_d + \gamma)\sin(2\psi_d),$$

$$D_v^+ = \frac{1}{4}[(1 + \cos^2\theta_d)\cos(2\phi_d - \gamma) - \sin^2\theta_d]\cos(2\psi_d)$$
$$+ \frac{1}{2}\cos\theta_d\sin(2\phi_d - \gamma)\sin(2\psi_d),$$

$$D_u^\times = \frac{1}{4}[\sin^2\theta_d - (1 + \cos^2\theta_d)\cos(2\phi_d + \gamma)]\sin(2\psi_d)$$
$$+ \frac{1}{2}\cos\theta_d\sin(2\phi_d + \gamma)\cos(2\psi_d),$$

$$D_v^\times = \frac{1}{4}[\sin^2\theta_d - (1 + \cos^2\theta_d)\cos(2\phi_d - \gamma)]\sin(2\psi_d)$$
$$+ \frac{1}{2}\cos\theta_d\sin(2\phi_d - \gamma)\cos(2\psi_d). \qquad (11)$$

The transfer function $\mathcal{T}$ is

$$\mathcal{T}(f, \hat{u} \cdot \hat{o}) = \frac{1}{2}\left\{\text{sinc}\left[\frac{f(1 - \hat{u} \cdot \hat{o})}{2f^*}\right]\exp\left[\frac{f(3 + \hat{u} \cdot \hat{o})}{2if^*}\right]\right.$$
$$\left. + \text{sinc}\left[\frac{f(1 + \hat{u} \cdot \hat{o})}{2f^*}\right]\exp\left[\frac{f(1 + \hat{u} \cdot \hat{o})}{2if^*}\right]\right\}, \qquad (12)$$

where $\text{sinc}(x) = \sin x/x$, $f^* = c/(2\pi L)$ is the transfer frequency of the detector, c is the speed of light, and L is the arm length of the detector. The frequency-domain GW signal $h_A(f)$ is

$$h_+(f) = \frac{M_z}{d_L}\sum_{\ell,m}A_{\ell m}Y_+^{\ell m}(\iota)I_a(\omega_{\ell m}, \tau_{\ell m}, \phi_{\ell m}),$$

$$h_\times(f) = \frac{M_z}{d_L}\sum_{\ell,m}A_{\ell m}Y_\times^{\ell m}(\iota)I_a\left(\omega_{\ell m}, \tau_{\ell m}, \phi_{\ell m} - \frac{\pi}{2}\right), \quad (13)$$

where I_a is given by Eq. (A1). For the detector II, the analytical frequency-domain detector signal is given by the replacement $\phi_d \rightarrow \phi_d - 2\pi/3$ in Eq. (8).

In the case of $10^7 M_\odot \leq M_z \leq 1.47 \times 10^9 M_\odot$, the damping time of the ringdown signals is from 10 minutes to one day with the frequencies of the four strongest modes within a few mHz. We choose to treat the Doppler shift $\exp[-2\pi i f\hat{o} \cdot \vec{r}_1/c]$, which comes from the time shift

between $\vec{r}_1$ (the position of SC_1) and the coordinate origin, as a constant, because f is within mHz, $|\vec{r}_1|/c = 1/3$ s, and the variation of $\vec{r}_1$ is small. We approximate $\mathcal{T}(f) \approx 1$ because the GW frequency is much less than the transfer frequency of TianQin, and take into account the rotation of TianQin, so $\hat{u}$ and $\hat{v}$ are

$$\hat{u} = \left[\cos\left(\omega_{tq}t - \frac{\gamma}{2}\right), \sin\left(\omega_{tq}t - \frac{\gamma}{2}\right), 0\right], \qquad \hat{v} = \left[\cos\left(\omega_{tq}t + \frac{\gamma}{2}\right), \sin\left(\omega_{tq}t + \frac{\gamma}{2}\right), 0\right], \qquad (14)$$

where $\omega_{tq} = 2\pi/T_{tq} = 1.99 \times 10^{-5}$ Hz is the rotation frequency of TianQin. For the detector I, the analytical frequency-domain detector signal is

$$
\begin{aligned}
s(f) = &\left[-\frac{\sin\gamma}{2}(1 + \cos^2\theta_d)\cos(2\psi_d)I_b(\phi_d, \omega_{\ell m}, \tau_{\ell m}, \phi_{\ell m})\right.\\
&\left.+ \sin\gamma\cos\theta_d\sin(2\psi_d)I_b\left(\phi_d + \frac{\pi}{4}, \omega_{\ell m}, \tau_{\ell m}, \phi_{\ell m}\right)\right]\frac{M_z A_{\ell m}}{d_L}Y_+^{\ell m}(\iota)\\
&+ \left[\frac{\sin\gamma}{2}(1 + \cos^2\theta_d)\sin(2\psi_d)I_b\left(\phi_d, \omega_{\ell m}, \tau_{\ell m}, \phi_{\ell m} - \frac{\pi}{2}\right)\right.\\
&\left.+ \sin\gamma\cos\theta_d\cos(2\psi_d)I_b\left(\phi_d + \frac{\pi}{4}, \omega_{\ell m}, \tau_{\ell m}, \phi_{\ell m} - \frac{\pi}{2}\right)\right]\frac{M_z A_{\ell m}}{d_L}Y_\times^{\ell m}(\iota). \qquad (15)
\end{aligned}
$$

Here I_b is given by Eq. (A2). For the detector II, the analytical frequency-domain detector signal is given by the replacement $\phi_d \rightarrow \phi_d - 2\pi/3$ in Eq. (15).

If a geocentric detector has a longer arm length than TianQin, it will have a longer rotation period and a lower transfer frequency than TianQin. Thus we only need to increase the boundary redshifted mass (we choose $10^7 M_\odot$ for TianQin) in the above two cases.

2. Heliocentric detectors

The heliocentric detector rotates around the Sun in the orbit of the Earth, with a fixed period of one year. We take LISA as an example, in the case of $10^5 M_\odot \leq M_z \leq 1.47 \times 10^9 M_\odot$, since the rotation frequency of LISA $\omega_{lisa} = 1.99 \times 10^{-7}$ Hz is extremely small, we ignore the rotation $\mathcal{T}$ of LISA. The arm vectors $\hat{u}$ and $\hat{v}$ are the same as Eq. (10), and the expressions for the frequency-domain detector signals are the same as Eqs. (8)–(13). This does not mean that LISA and TianQin will have the same detector signal, because the two detectors have different detector parameters $(\theta_d, \phi_d, \psi_d)$ for the same source $(\theta_s, \phi_s, \psi_s)$ (Appendix B), different transfer frequency, different noise, etc.

D. The noise curve

In this paper, we use the noise curve [93]

$$P_n(f) = \frac{S_x}{L^2} + \frac{2[1 + \cos^2(f/f^*)]S_a}{(2\pi f)^4 L^2}[1 + (0.4 \text{ mHz}/f)^2], \qquad (16)$$

where S_x is the position noise, S_a is the acceleration noise, L is the arm length, $f^* = c/(2\pi L)$ is the transfer frequency

of the detector. For LISA, $S_x = (1.5 \times 10^{-11} \text{ m})^2 \text{ Hz}^{-1}$, $S_a = (3 \times 10^{-15} \text{ ms}^{-2})^2 \text{ Hz}^{-1}$, $L = 2.5 \times 10^9$ m and $f^* = 19.09$ mHz [20]. For TianQin, $S_x = (10^{-12} \text{ m})^2 \text{ Hz}^{-1}$, $S_a = (10^{-15} \text{ ms}^{-2})^2 \text{ Hz}^{-1}$, $L = \sqrt{3} \times 10^8$ m and $f^* = 0.2755$ Hz [21]. For Taiji, $S_x = (8 \times 10^{-12} \text{ m})^2 \text{ Hz}^{-1}$, $S_a = (3 \times 10^{-15} \text{ ms}^{-2})^2 \text{ Hz}^{-1}$, $L = 3 \times 10^9$ m and $f^* = 15.90$ mHz [46].

For LISA and Taiji, we also add the confusion noise [93]

$$
\begin{aligned}
S_c(f) = &\frac{2.7 \times 10^{-45} f^{-7/3}}{1 + 0.6(f/0.01909)^2}e^{-f^{0.138}-221f\sin(521f)}\\
&\times [1 + \tanh(1680(0.00113 - f))] \text{ Hz}^{-1}, \qquad (17)
\end{aligned}
$$

to the noise curve.

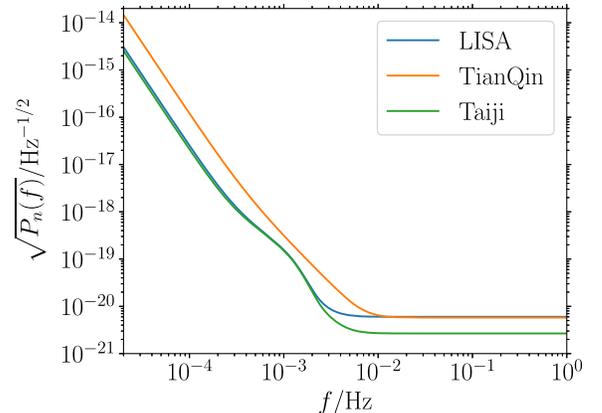Figure 3 shows the noise power spectra of LISA, TianQin, and Taiji.

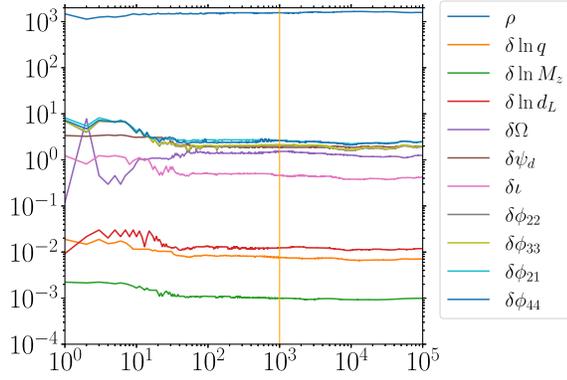FIG. 3.   The noise power spectra of LISA, TianQin, and Taiji.

FIG. 4. The effect of the number of simulated sources on the median errors of the parameter estimation and source localization with LISA for the binary with $10^6 \, M_\odot$ at $z = 1$. The vertical orange solid line represents the number of simulated sources that we choose to obtain the median error of each parameter.

E. Fisher information matrix

For convenience, we define the inner product of two frequency-domain signals $s_1(f)$ and $s_2(f)$ as

$$(s_1|s_2) = 2 \int_{f_{\text{in}}}^{f_{\text{out}}} \frac{s_1(f)s_2^*(f) + s_1^*(f)s_2(f)}{P_n(f)} df. \quad (18)$$

The SNR ρ is simply defined as

$$\rho^2 = (s|s). \quad (19)$$

For a detected source with a significant SNR (a threshold of $\rho \geq 8$), we can use the FIM method to estimate its parameters, which is defined as

$$\Gamma_{ij} = \left(\frac{\partial s(f)}{\partial \boldsymbol{\xi}_i} \middle| \frac{\partial s^*(f)}{\partial \boldsymbol{\xi}_j} \right), \quad (20)$$

where $\boldsymbol{\xi} = \{q, M_z, d_L, \theta_d, \phi_d, \psi_d, \iota, \phi_{22}, \phi_{33}, \phi_{21}, \phi_{44}\}$ spans the 11-dimensional parameter space. Although the ringdown phases $\phi_{\ell m}$ are related to the source parameters and the specific process, the relationship is not well known. Thus we treat $\phi_{\ell m}$ as four independent parameters.

The covariance matrix of these parameters is

$$\sigma_{ij} = \langle \Delta \xi^i \Delta \xi^j \rangle \approx (\Gamma^{-1})_{ij}. \quad (21)$$
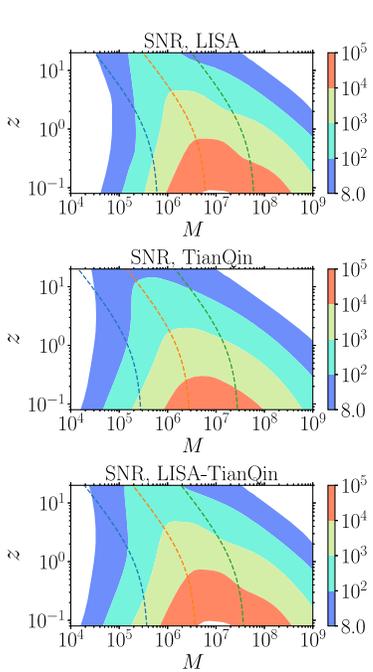

FIG. 5. The median SNRs of TianQin and LISA with ringdown signals from binaries with different total masses and different redshifts. For LISA, the blue, orange, and green dashed lines correspond to the redshifted masses $M_z = 6.5 \times 10^5 \, M_\odot$, $6.5 \times 10^6 \, M_\odot$ and $6.5 \times 10^7 \, M_\odot$, respectively. For TianQin, the blue, orange, and green dashed lines correspond to the redshifted masses $M_z = 3 \times 10^5 \, M_\odot$, $3 \times 10^6 \, M_\odot$ and $3 \times 10^7 \, M_\odot$, respectively. For LISA-TianQin network, the blue, orange, and green dashed lines correspond to the redshifted masses $M_z = 4 \times 10^5 \, M_\odot$, $4 \times 10^6 \, M_\odot$ and $4 \times 10^7 \, M_\odot$, respectively.
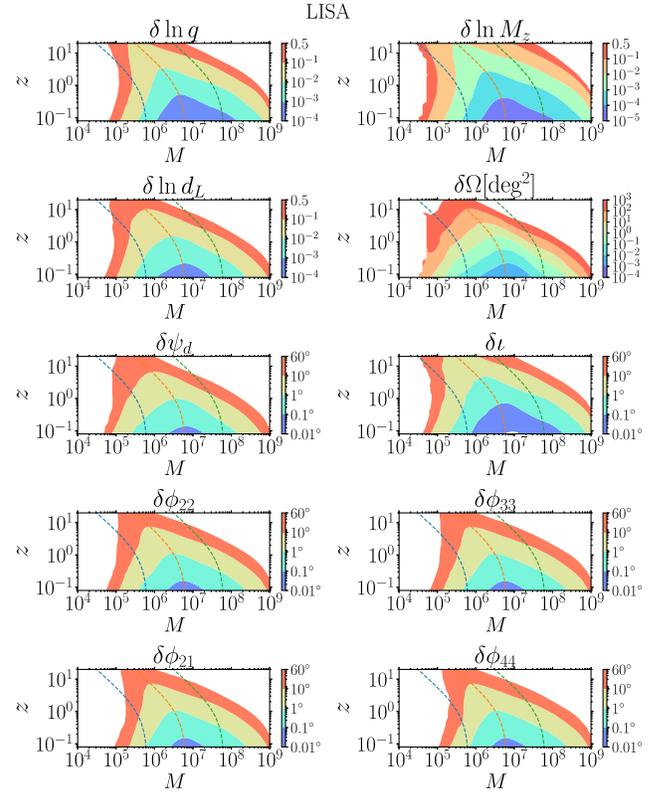

FIG. 6. The median errors of the parameter estimation and source localization of LISA with ringdown signals from binaries with different masses and different redshifts. The blue, orange, and green dashed lines correspond to the redshifted masses $M_z = 6.5 \times 10^5 \, M_\odot$, $6.5 \times 10^6 \, M_\odot$ and $6.5 \times 10^7 \, M_\odot$, respectively.

The angular uncertainty of the sky localization is evaluated as

$$\Delta\Omega_s \equiv 2\pi \sin\theta_d \sqrt{\sigma_{\theta_d\theta_d}\sigma_{\phi_d\phi_d} - \sigma^2_{\theta_d\phi_d}}, \qquad (22)$$

so the probability that the source lies outside an error ellipse enclosing the solid angle $\Delta\Omega$ is simply $e^{-\Delta\Omega/\Delta\Omega_s}$.

III. PARAMETER ESTIMATION AND SOURCE LOCALIZATION

It is hard to control the noise of space-based detectors below the frequency $\sim 2 \times 10^{-5}$ Hz [73], so we take 2×10^{-5} Hz as the lower cutoff frequency. For BH binaries with the redshifted total mass $M_z \geq 10^9 \ M_\odot$, f_{22} and f_{21} are out of the frequency band of space-based detectors, thus we do not consider binaries with the total mass $M \geq 10^9 \ M_\odot$. For ringdown signals, we set $f_{in} = \max(0.5f_{21}, 2 \times 10^{-5} \text{ Hz})$ and $f_{out} = 2f_{44}$. Since higher frequencies correspond to higher overtones and higher harmonics, which are not used in our computation, we choose this upper limit f_{out} in the

integration. The lower limit in the integration stands for the starting frequency of the ringdown stage, and we set it to be $0.5f_{22}$ in our computation.

In this section, for each binary with the same total mass and redshift, we use Monte Carlo simulation to generate 1000 sources and obtain the median error of each parameter. We also check the effect of the number of simulated sources on the median errors and the results are shown in Fig. 4. We see that the results are almost the same if the number of simulated sources is larger than 100, so we choose to simulate 1000 sources. From Eqs. (3), (8), (11), and (15), we see that there exists a transformation of extrinsic parameters yielding an exact degeneracy, called reflected sky position (for a reflection with respect to the detector plane) [76],

$$\theta_d \to \pi - \theta_d,$$

$$\iota \to \pi - \iota,$$

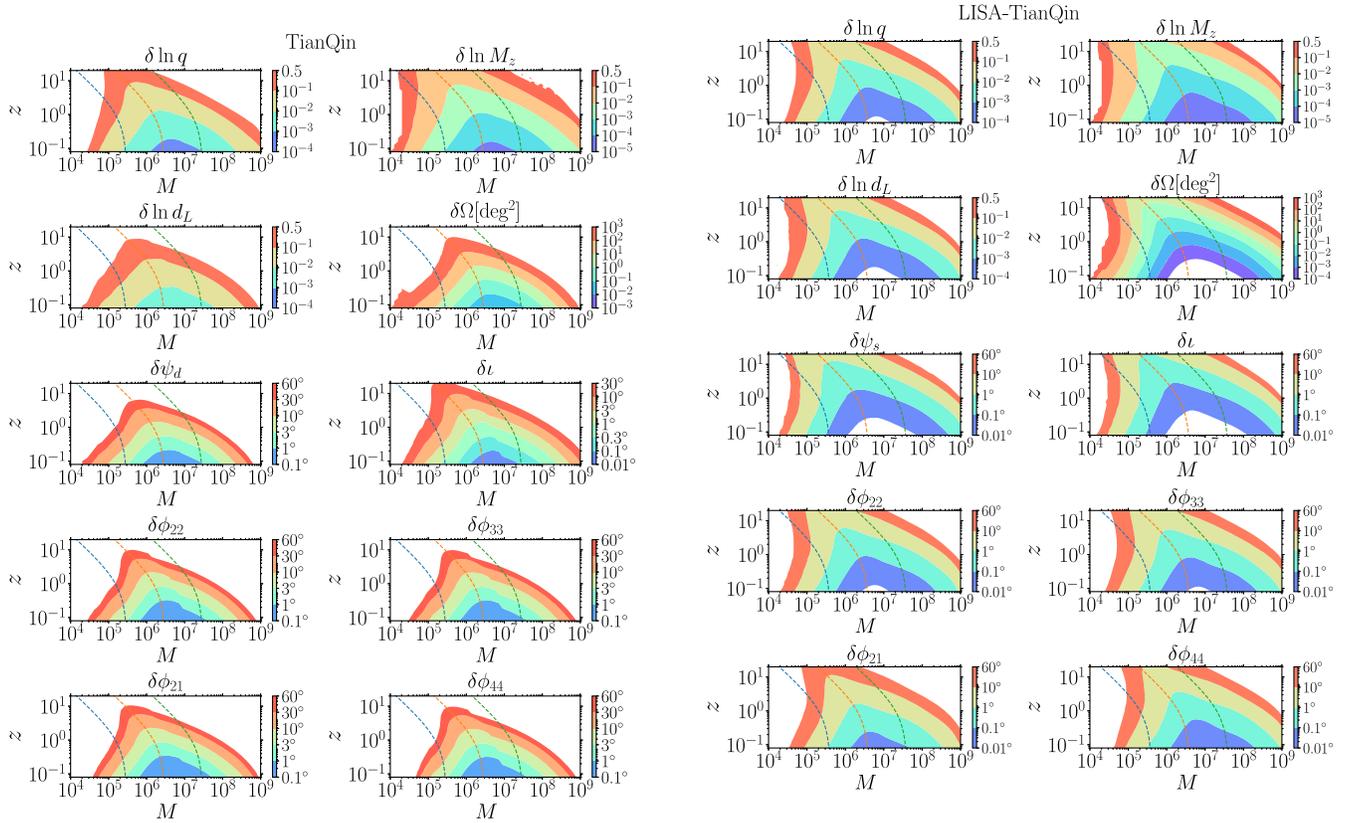$$\psi_d \to \pi - \psi_d. \qquad (23)$$

FIG. 7. The median errors of the parameter estimation and source localization of TianQin with ringdown signals from binaries with different masses and different redshifts. The blue, orange, and green dashed lines correspond to the redshifted masses $M_z = 3 \times 10^5 \ M_\odot$, $3 \times 10^6 \ M_\odot$ and $3 \times 10^7 \ M_\odot$, respectively. In the case of $M_z \geq 10^7 \ M_\odot$, we take the rotation of TianQin into account and adopt the low-frequency approximation.

FIG. 8. The median errors of the parameter estimation and source localization of the network of LISA and TianQin with ringdown signals from binaries with different masses and different redshifts. The blue, orange, and green dashed lines correspond to the redshifted masses $4 \times 10^5 \ M_\odot$, $4 \times 10^6 \ M_\odot$ and $4 \times 10^7 \ M_\odot$, respectively. In the case of $M_z \geq 10^7 \ M_\odot$, we take the rotation of TianQin into account and adopt the low-frequency approximation.

Thus, in general, there are two degenerate positions in the sky in the parameter estimation with ringdown signals. Moreover, in the low-frequency limit, due to $\mathcal{T} \to 1$, the constraints on $\hat{u} \cdot \hat{o}$ and $\hat{v} \cdot \hat{o}$ in the transfer function become weak, leading to another transformation [76],

$$\phi_d \to \phi_d + \frac{k\pi}{2} \quad \mathrm{mod} \ 2\pi,$$

$$\psi_d \to \psi_d + \frac{k\pi}{2} \quad \mathrm{mod} \ \pi, \qquad (24)$$

where $k = 0, 1, 2, 3$. The new transformation implies that, in the parameter estimation with ringdown signals from supermassive BH binaries, there are eight degenerate positions in the sky in the low-frequency limit. Note that the two transformations (23) and (24) lead to a multimodal distribution in the Bayesian analysis discussed in the next section, but they are missed in the FIM analysis. The parameter distribution of simulated sources is shown in Appendix C.

Using a typical source with $M = 10^7 \ M_\odot$ and $z = 1$, we analyze the dependence of these errors on the sky position. We also explore the capability of source localization for different detectors and their combined network. The median SNR for the simulated sources is shown in Fig. 5 and the results for the parameter estimation are shown in Figs. 6, 7, 8, 9, 10, and Tables II and III. The results with Taiji are similar to those with LISA.

Figure 6 shows the median errors of the parameter estimation and source localization of LISA with ringdown signals from binaries with different total masses and different redshifts, and Fig. 7 shows the median errors of the parameter estimation and source localization of TianQin. For BH binaries with the total mass $M \geq 10^4 \ M_\odot$, as the total mass increases, the SNR of its ringdown signal will exceed the threshold $\rho = 8$, the estimation errors of $\delta \ln q$, $\delta \ln M_z$ and $\delta \ln d_L$ will be within 0.5, the estimation errors of the angles and phases will be within 60°, and the source localization will be within 1000 deg². If its total mass $M \geq 10^5 \ M_\odot$, in most cases, the SNR of its ringdown
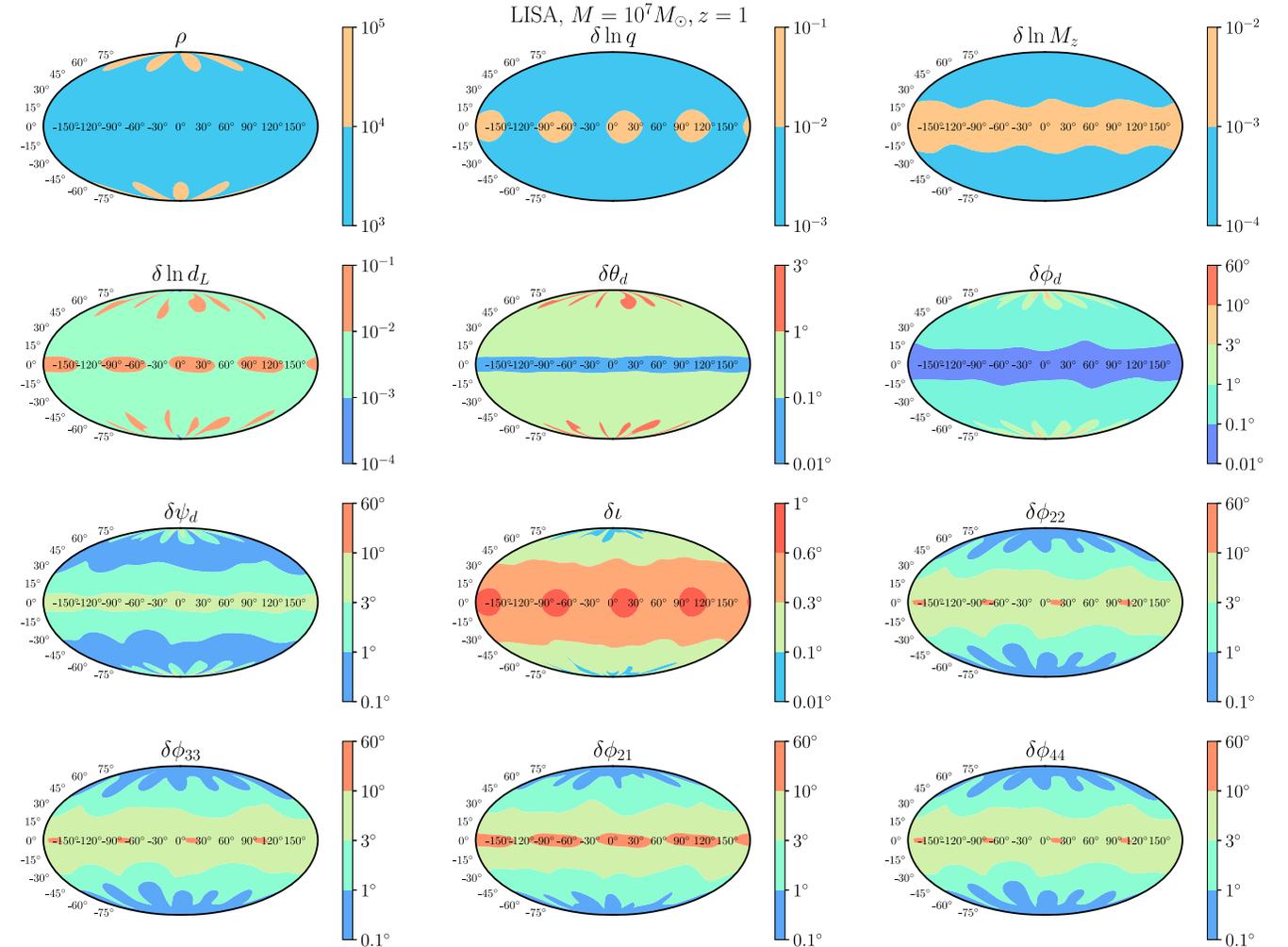

FIG. 9. The sky map of the parameter estimation and source localization with LISA for the binary with the total mass $M = 10^7 \ M_\odot$ at $z = 1$. Note that LISA is put in the equatorial plane. The other source parameters are $q = 2, \psi_d = 60°, \iota = 45°$, and $\phi_{\ell m} = 0°$.

signal will be larger than 100, the estimation errors of $\delta \ln q$ and $\delta \ln d_L$ will be within 0.1, the estimation error of $\delta \ln M_z$ will be within 0.01, the estimation errors of the angles and phases will be within 10°, and the source localization will be within 10 deg². If its total mass $M \geq 10^6 \, M_\odot$, the SNR can exceed $\sim 10^3$, the estimation errors of $\delta \ln q$ and $\delta \ln d_L$ will be within 0.01, the estimation error of $\delta \ln M_z$ will be within 0.001, the estimation errors of the angles and phases will be within 1°, and the source localization will be within 1 deg². Figure 8 shows the median errors of the parameter estimation and source localization with the network of LISA and TianQin, which implies that the network can improve the parameter estimation by about one order of magnitude, and can improve the source localization by two or even three orders of magnitude compared with individual detector. Figures 5, 6, 7, and 8 tell us that for BH binaries at the same distance, LISA has larger SNR and better parameter estimation and source localization for the BH binary with $M_z = 6.5 \times 10^6 \, M_\odot$, TianQin has larger

SNR and better parameter estimation and source localization for the BH binary with $M_z = 3 \times 10^6 \, M_\odot$, the network of LISA and TianQin has larger SNR and better parameter estimation and source localization for the BH binary with $M_z = 4 \times 10^6 \, M_\odot$.

There are three main factors that affect the source localization. The first factor is the relative difference of the source location between the detector I and the detector II. We use the angle between the direction (θ_d, ϕ_d) and the direction $(\theta_d, \phi_d - 2\pi/3)$ to represent the difference, which reaches the maximum at $\theta_d = \pi/2$ and reaches the minimum at $\theta_d = \{0, \pi\}$. The second factor is the transfer function $\mathcal{T}$. For the ringdown frequency $0.5 f^* \leq f \leq 5 f^*$, $\mathcal{T}$ slightly weakens the response and dramatically improves the source localization. For the ringdown frequency $f \geq 10 f^*$, $\mathcal{T}$ significantly weakens the response and the estimation of all parameters. For the ringdown frequency $f \leq 0.1 f^*$, $\mathcal{T}$ contributes little to the source localization because $\mathcal{T} \to 1$. Thus the transfer function of LISA can improve their source localization
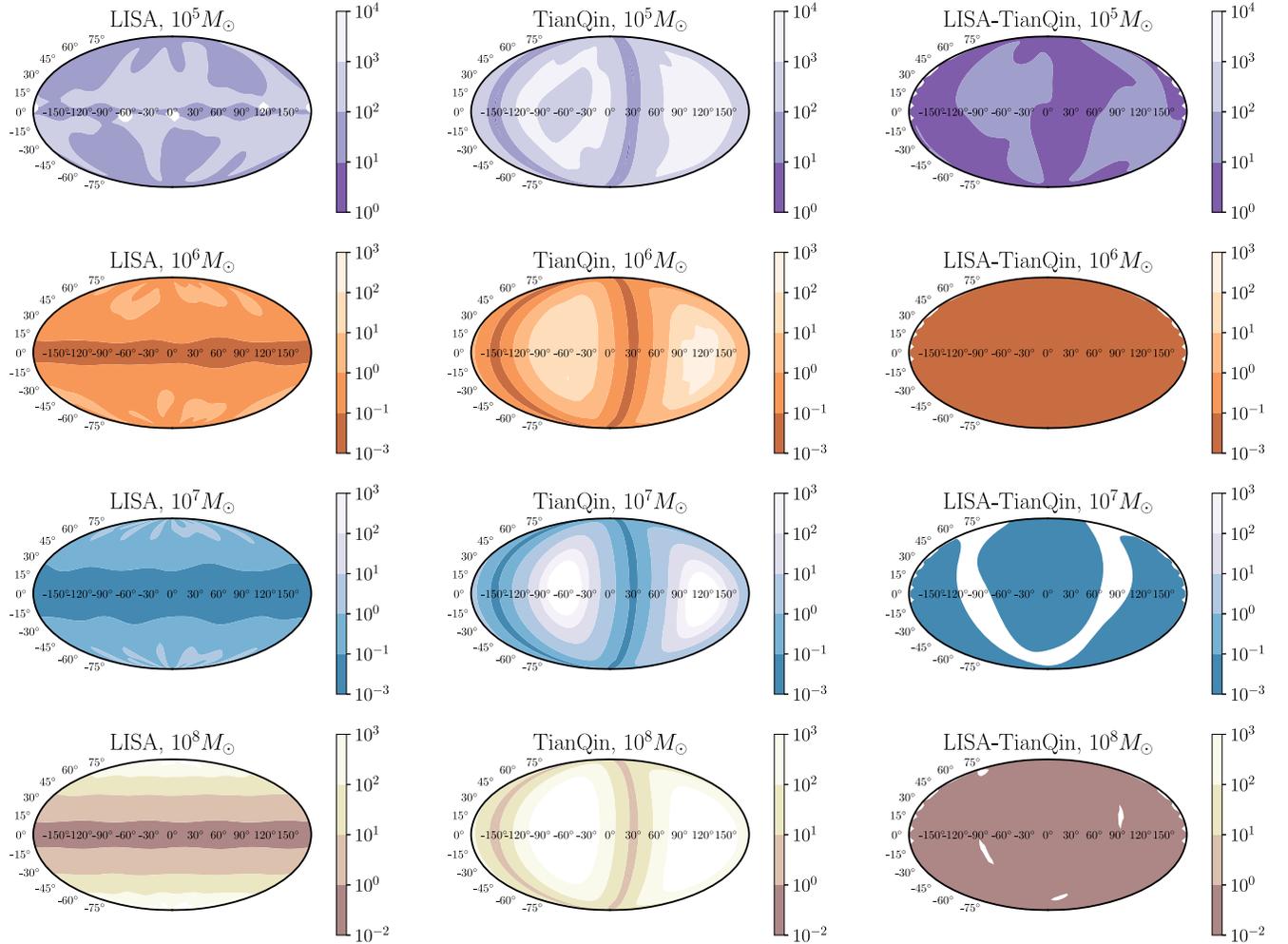

FIG. 10.   The sky map of source localization with LISA, TianQin, and their combined network for binaries with total masses $10^5 \, M_\odot$, $10^6 \, M_\odot$, $10^7 \, M_\odot$, and $10^8 \, M_\odot$ at $z = 1$. The other source parameters are $q = 2, \psi_d = \pi/3, \iota = \pi/4$, and $\phi_{\ell m} = 0$.

for binaries with the redshifted total masses $1.7 \times 10^5 \, M_\odot \leq M_z \leq 1.7 \times 10^6 \, M_\odot$. The transfer function of Taiji can improve its source localization for the binary with the redshifted total mass $2 \times 10^5 \, M_\odot \leq M_z \leq 2 \times 10^6 \, M_\odot$. The transfer function of TianQin can improve its source localization for the binary with the redshifted total mass $1.2 \times 10^4 \, M_\odot \leq M_z \leq 1.2 \times 10^5 \, M_\odot$. The third factor is the different responses of the detector to different QNMs. In one LIGO-like detector, because of $Y_{+,\times}^{\ell\ell} \propto (\sin \iota)^{\ell-2} Y_{+,\times}^{22}$, the response difference between the $(2, 1)$ mode and the $(2, 2)$ mode is bigger than those from $(3, 3)$ and $(4, 4)$ modes. However, the difference is still not big enough for one LIGO-like detector to localize the source. Thus, for the source localization of each space-based GW detector, we need to consider both the detector I and II.

Figure 9 shows the dependence of these errors on the sky position for LISA. Note that we place LISA in the x-y plane, i.e., the equatorial plane. For the LISA-TianQin network, we set LISA pointing to $(\theta_s, \phi_s) = (\pi/3, 0)$. For the LISA-TianQin-Taiji network (3-network), we set Taiji pointing to $(\theta_s, \phi_s) = (\pi/3, 0)$, and set LISA pointing to $(\theta_s, \phi_s) = (\pi/3, -2\pi/9)$. Fig. 9 implies that the angular resolution becomes the best for sources along the detector plane, where the relative difference of source location reaches the maximum, but it is the worst for sources locating perpendicular to the detector plane, where the relative difference of source location reaches the minimum.

The tensor response of a detector reaches the minimum at its angular bisector and the vertical direction of its angular bisector in the detector plane [94–96], which is at the longitude of $\{-90°, 0°, 90°, 180°\}$ in the equatorial plane for the detector I, and at the longitude of $\{-150°, -60°, 30°, 120°\}$ in the equatorial plane for the detector II. The tensor response of a detector reaches the maximum at the direction perpendicular to the detector plane, which is near the two poles. Thus, except $\{\theta_d, \phi_d\}$, the worst accuracy of the parameter estimation generally occurs for sources along the detector plane, where the tensor response reaches the minimum, and the best accuracy of the parameter estimation generally occurs for sources along the two poles, where the tensor response reaches the maximum. However, as $\theta_d \to 0$, both $\hat{u} \cdot \hat{o}$ and $\hat{v} \cdot \hat{o}$ in $\mathcal{T}$ go to 0, so $\mathcal{T}$ contributes little to the estimation

TABLE II. Median localization errors of different detectors with ringdown signals from binaries with total masses $\{10^5, 10^6, 10^7, 10^8, 10^9\} M_\odot$ at the redshift $z = 1$.

$M(M_\odot)$	LISA	TianQin	Taiji	LISA-TianQin	3-network
10^5	139.87	2122.59	30.00	14.21	4.24
10^6	1.53	10.97	0.243	0.00645	0.00276
10^7	1.00	11.36	0.544	0.00303	0.000745
10^8	160.95	1180.32	113.61	0.108	0.0211
10^9	$>10^5$	$>10^5$	$>10^5$	80.13	12.99

TABLE III. Median localization errors of different detectors with ringdown signals from binaries with total masses $\{10^5, 10^6, 10^7, 10^8, 10^9\} M_\odot$ at the redshift $z = 3$.

$M(M_\odot)$	LISA	TianQin	Taiji	LISA-TianQin	3-network
10^5	252.90	4893.65	45.72	16.26	5.60
10^6	9.09	62.97	1.78	0.033	0.0101
10^7	103.99	458.02	82.27	0.112	0.0415
10^8	18963	$>10^5$	13191	9.50	1.518
10^9	$>10^5$	$>10^5$	$>10^5$	$>10^5$	$>10^5$

of ϕ_d. Furthermore, from Eq. (11), we see that ϕ_d and ψ_d degenerates into one parameter $\phi_d - \psi_d$ when $\theta_d = 0$ due to the coupling. Thus the estimation of ψ_d becomes the worst for binaries along the two poles.

Figure 10 shows the dependence of the source localization on the sky position with the ringdown signal for LISA, TianQin, and their combined network. The combined network of two detectors not only improves the localization accuracy but also makes the sky map more uniform. Tables II and III show the median localization errors of different detectors with ringdown signals from binaries with total masses $\{10^5, 10^6, 10^7, 10^8, 10^9\} M_\odot$ at the redshift $z = 1$ and the redshift $z = 3$ respectively. From
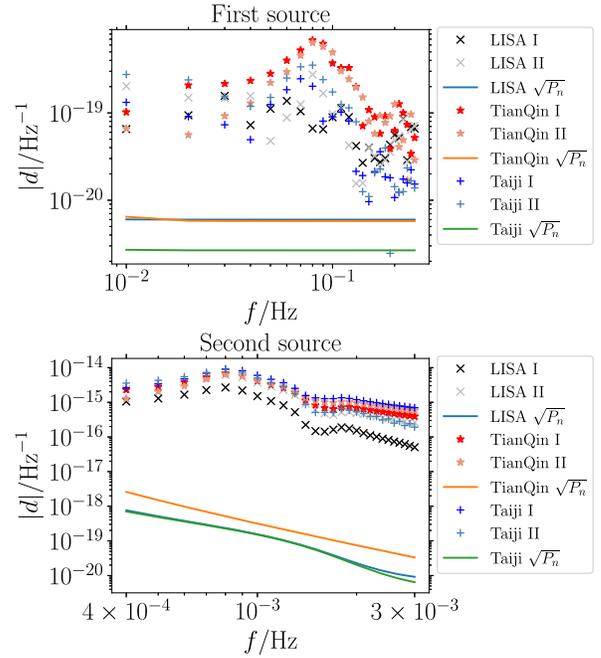

FIG. 11. The amplitudes of the strain data in LISA, TianQin, and Taiji for the two sources. The first source has the total mass $M = 10^5 \, M_\odot$. The sampling frequency and the observation time are set to be 1 Hz and 100 s respectively. The second source has the total mass $M = 10^7 \, M_\odot$. The sampling frequency and the observation time are set to be 0.1 Hz and 10000 s respectively. The other parameters of the two sources are $q = 2$, $z = 1$, $\theta_s = \phi_s = \psi_s = \phi_{\ell m} = \pi/3$ and $\iota = \pi/4$.

the two tables, we see that Taiji has better source localization than LISA and TianQin due to its lower noise curve for massive BH binaries and lower transfer frequency for supermassive BH binaries. As the total mass of the BH binary increases, the improvement in the source localization is one to three orders for the LISA-TianQin network compared with individual detector. The 3-network improves the sky localization only a few times than the LISA-TianQin network.

Reference [76] analyzes two binaries with $M = 4 \times 10^5 \ M_\odot$, $q = 3$ and $z = 4$, using Bayesian inference method, and the localization errors are about 200 square degrees, which are consistent with the median error 80 square degrees given in Fig. 6. Reference [77] analyzes five binaries with $M = 2 \times 10^6 \ M_\odot$, $q = 3$ and $z = 4$, using Bayesian inference method and the PhenomHM waveform with higher-order harmonic modes and aligned spins. The localization errors of the five sources are about
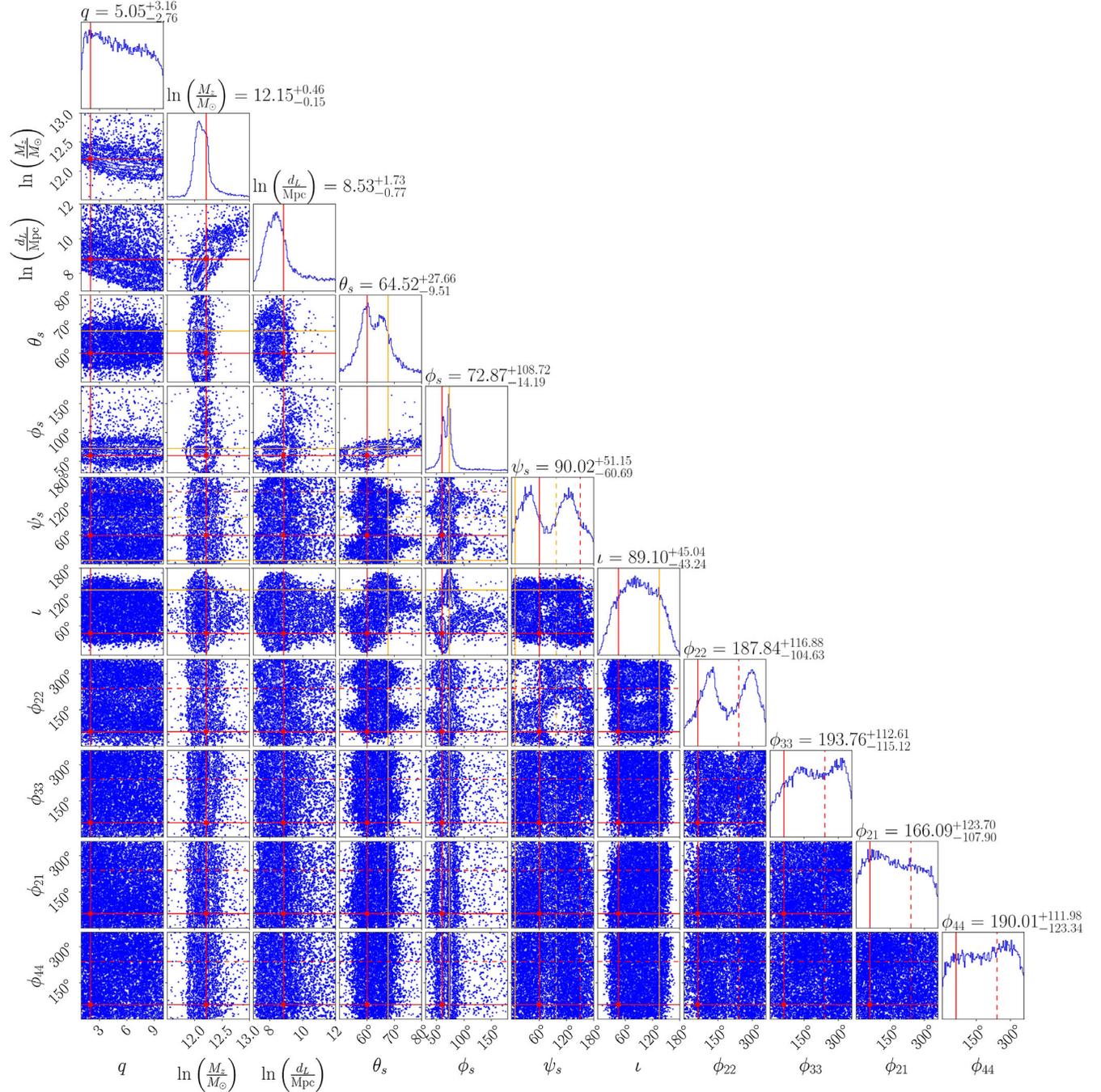

FIG. 12.   The posterior distribution for the first source with LISA. The red solid lines (dots) represent the true parameters, the orange solid lines represent the reflected sky position given by Eq. (23), and the dashed lines represent the degenerate points given by Eq. (27).

0.001 square radians or 3 square degrees, which are consistent with the median error 1 square degree given in Fig. 6. The localization errors of the binary with $M = 4 \times 10^7\ M_\odot$, $q = 5$ and $z = 2$, and the binary with $M = 3 \times 10^5\ M_\odot$, $q = 1.4$ and $z = 7$, are about 2000 and 800 square degrees respectively, which are roughly consistent with the median error 500 square degrees given in Fig. 6. In Ref. [73], they use the low-frequency limit and found that the estimation errors for $q = 10$ are a few times worse than those for $q = 2$ which are consistent with the results shown in Fig. 1. In the low-frequency limit, the transfer function is independent of the frequency, so there are eight degenerate sky positions in the localization contours [73]. In this paper, we consider the frequency dependence of the transfer function and use it to improve the sky localization. As we will see in the next
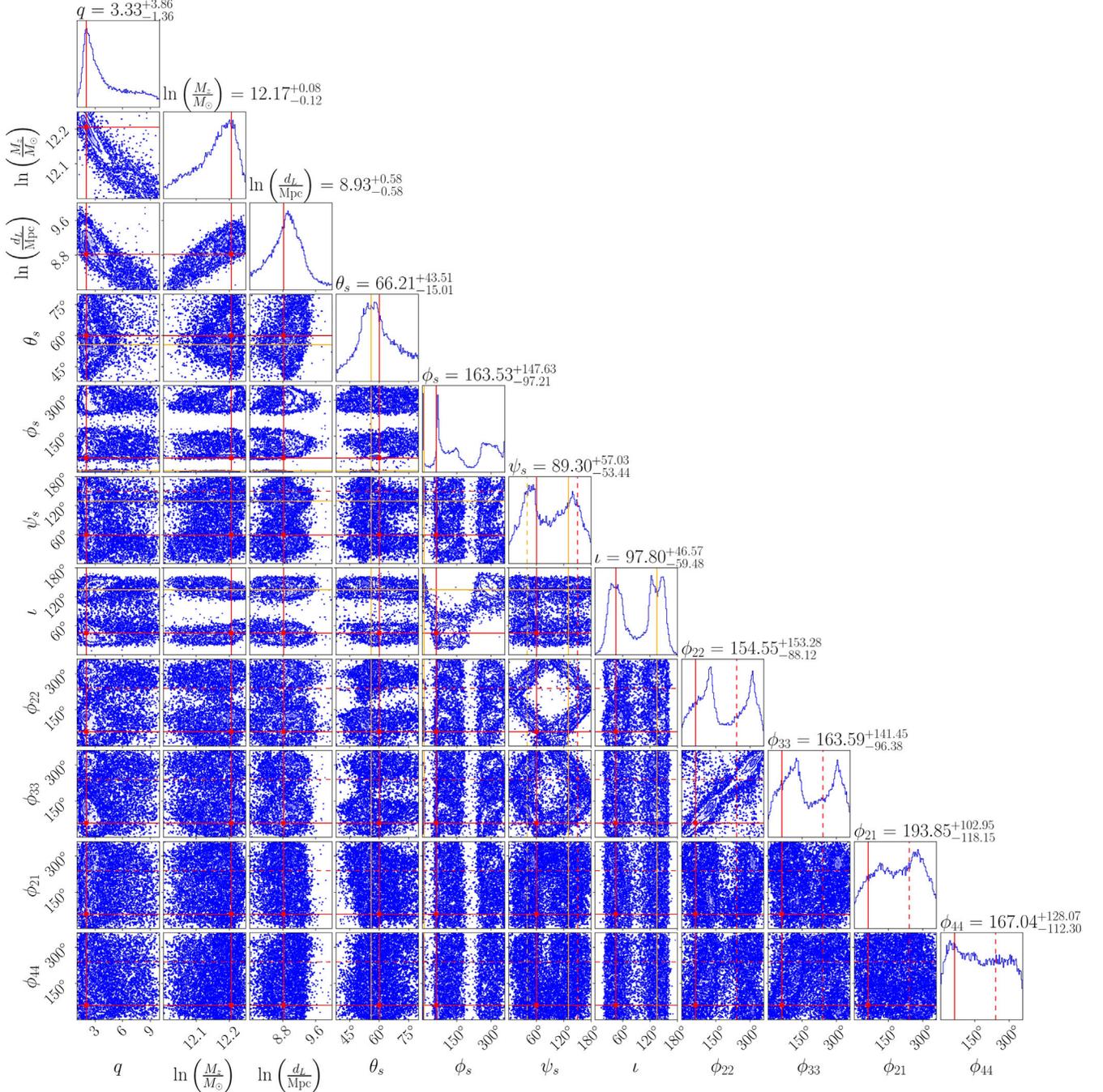

FIG. 13. The posterior distribution for the first source with TianQin. The red solid lines (dots) represent the true parameters, the orange solid lines represent the reflected sky position given by Eq. (23), and the dashed lines represent the degenerate points given by Eq. (27).

section, the transfer function also helps to break the eight degeneracy (24).

IV. BAYESIAN INFERENCE

To check the FIM results, we use Bayesian inference method to analyze two specific sources and compare the FIM results with those from Bayesian analysis.

Bayesian inference method is based on Bayes rule

$$p(\boldsymbol{\xi}|d) = \frac{p(d|\boldsymbol{\xi})p(\boldsymbol{\xi})}{p(d)}, \tag{25}$$

where $p(\boldsymbol{\xi}|d)$ is the posterior distribution of the parameters $\boldsymbol{\xi}$, $p(d|\boldsymbol{\xi})$ is the likelihood,
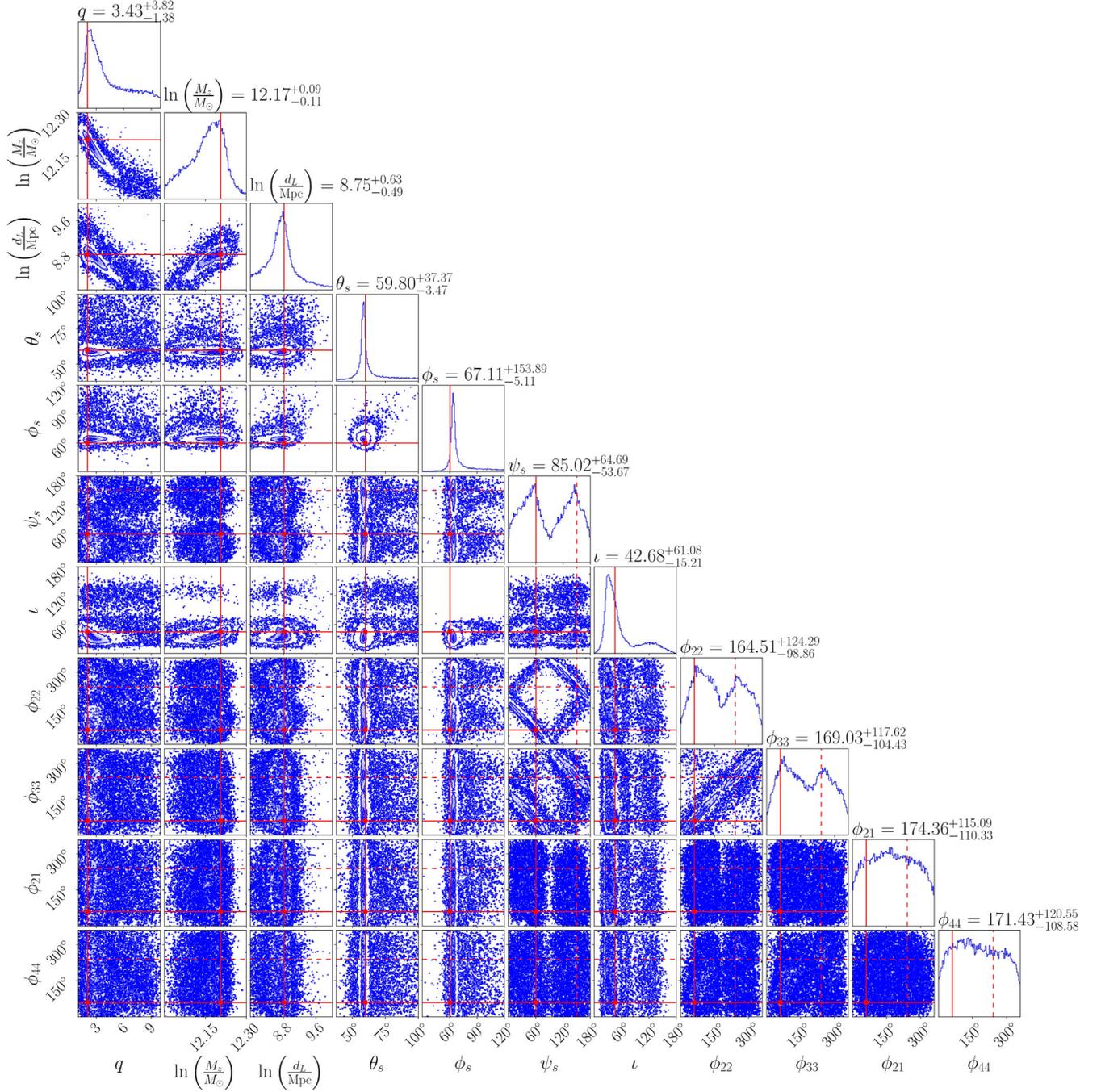

FIG. 14. The posterior distribution for the first source with the network of LISA and TianQin. The red solid lines (dots) represent the true parameters, the orange solid lines represent the reflected sky position given by Eq. (23), and the dashed lines represent the degenerate points by Eq. (27).

$$p(d|\boldsymbol{\xi}) = \exp\left[-\frac{1}{2}(s(\boldsymbol{\xi}) - d|s(\boldsymbol{\xi}) - d)\right], \quad (26)$$

$d = s(\boldsymbol{\xi_0}) + n$ is the observed data for the true parameters $\boldsymbol{\xi_0}$, n is the noise generated by the noise power spectra, $p(\boldsymbol{\xi})$ is the prior distribution of the parameters $\boldsymbol{\xi}$, and $p(d)$ is the evidence which is treated as a normalization constant. For the two sources, we choose the sampler Dynesty [97] with

"mulit" bound and "rwalk" sample method for nested sampling [98,99], to obtain the posterior distribution of the parameters $\boldsymbol{\xi}$.

We choose the two sources with different SNRs. The parameters of the first source with smaller SNR are $q = 2$, $M = 10^5 M_{\odot}$, $z = 1$, $\theta_s = \phi_s = \psi_s = \phi_{\ell m} = \pi/3$, and $\iota = \pi/4$. The number of live points of the sampler, the sampling frequency, and the observation time are set to be
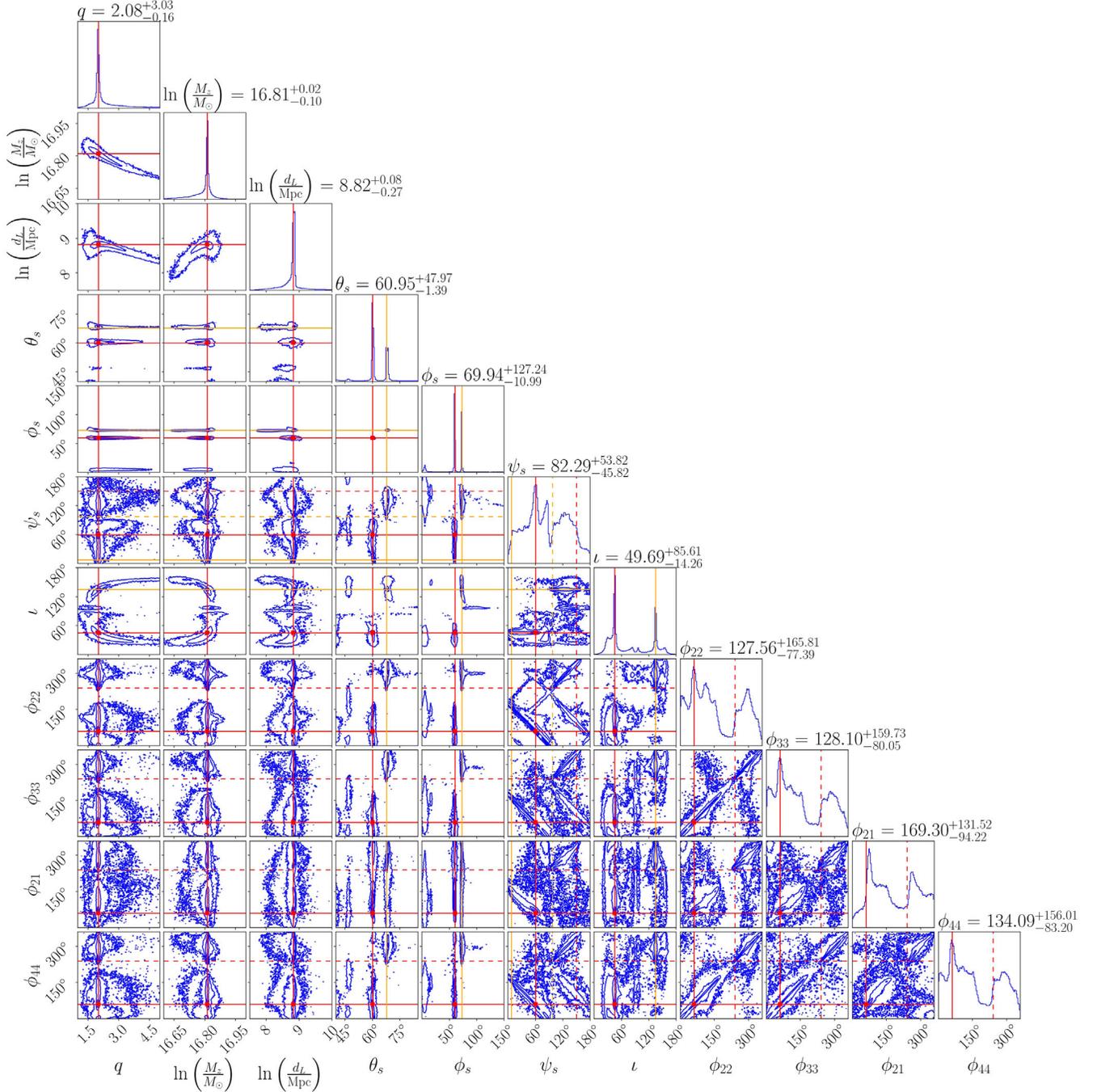

FIG. 15.   The posterior distribution for the second source with LISA. The red solid lines (dots) represent the true parameters, the orange solid lines represent the reflected sky position given by Eq. (23), and the dashed lines represent the degenerate points given by Eq. (27).

1500, 1 Hz, and 100 s, respectively. The parameters of the second source with larger SNR are $q = 2$, $M = 10^7 \, M_\odot$, $z = 1$, $\theta_s = \phi_s = \psi_s = \phi_{\ell m} = \pi/3$, and $\iota = \pi/4$. The number of live points of the sampler, the sampling frequency, and the observation time are set to be 3000, 0.1 Hz, and 10000 s, respectively. We choose $\iota = \pi/4$ because in this case the parameter errors are close to the median errors. From Eq. (23), we see that in the heliocentric coordinate, the sky position $(\theta_s, \phi_s, \psi_s, \iota) = (60°, 60°, 60°, 45°)$ is reflected to $(67.7°, 72.8°, 7.2°, 135°)$ for LISA, and to $(55.7°, 6.3°, 130°, 135°)$ for TianQin.

The amplitudes of the strain data in LISA, TianQin, and Taiji for the two sources are shown in Fig. 11. From Fig. 11, we see a high peak which corresponds to the modes (2, 2) and (2, 1), and a low peak behind the high peak which corresponds to the modes (3, 3) and (4, 4). If we work in the
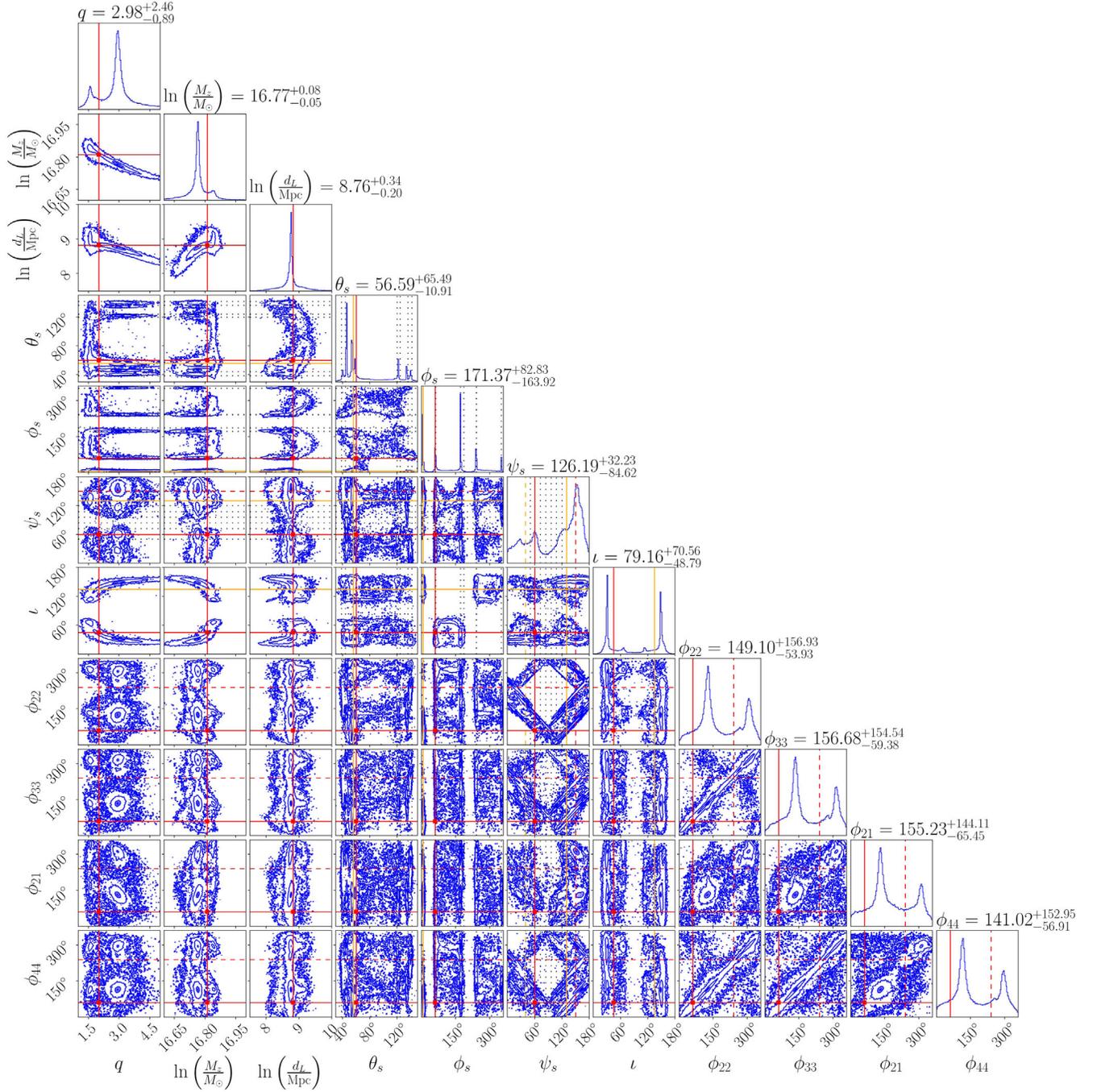

FIG. 16. The posterior distribution for the second source with TianQin. The red solid lines (dots) represent the true parameters, the orange solid lines represent the reflected sky position given by Eq. (23), the black dotted lines represent the degenerate points given by Eq. (24), and the dashed lines represent the degenerate points given by Eq. (27).

heliocentric coordinate, from Eqs. (5) and (6), we find that the phases of GW signals have the degeneracy

$$s(\psi_s, \phi_{\ell m}) = s(\psi_s \pm \pi) = s(\psi_s \pm \pi/2, \phi_{\ell m} \pm \pi), \quad (27)$$

which is not apparent if we work in the detector coordinate. Thus, all the posterior distributions of $\phi_{\ell m}$ at least have two peaks. We set the prior distributions of the parameters

$\{q, \ln(M/M_\odot), \ln(d_L/\text{Mpc}), \cos\theta_s, \phi_s, \psi_s, \cos\iota, \phi_{\ell m}\}$ to be uniform in the ranges [1, 10], [11.5, 20.72], [6.2, 20.34], [−1, 1], [0, 2π], [0, π], [−1, 1], and [0, 2π], respectively. The results of Bayesian analysis are shown in Figs. 12, 13, 14, 15, 16, and 17. The Bayesian results with Taiji are similar to those with LISA, and the results with the 3-network are a few times better than those with the network of LISA and TianQin.
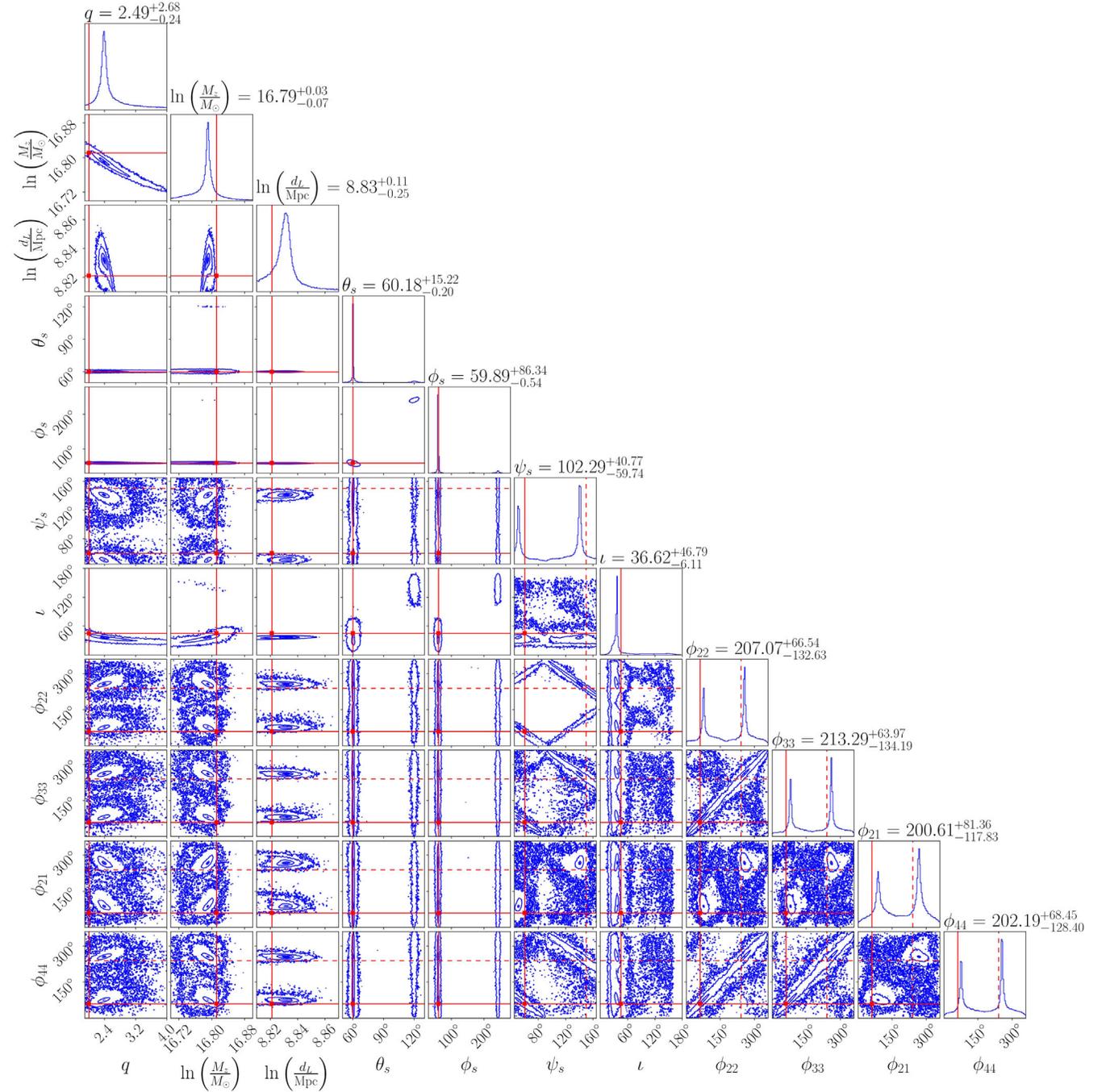

FIG. 17. The posterior distribution for the second source with the network of LISA and TianQin. The red solid lines (dots) represent the true parameter values, the orange solid lines represent the reflected sky position given by Eq. (23), and the dashed lines represent the degenerate points given by Eq. (27).

For the first source, from Figs. 12, 13 and 14, the errors $\{\delta\theta_s, \delta\phi_s\}$ with LISA, TianQin and the network of LISA and TianQin are $\{15°, 34°\}$, $\{25°, 81°\}$ and $\{13°, 27°\}$, respectively, which are a few times worse than the median errors $\{6.4°, 4.8°\}$, $\{16.8°, 20.1°\}$ and $\{1.4°, 2.4°\}$ with the FIM method given by Figs. 6, 7 and 8. For the second source, from Figs. 15, 16 and 17, the errors $\{\delta\theta_s, \delta\phi_s\}$ with LISA, TianQin and the network of LISA and TianQin are $\{6°, 9°\}$, $\{15°, 32°\}$ and $\{0.3°, 0.5°\}$, respectively, which are about one order worse than the median errors $\{0.5°, 0.6°\}$, $\{1.6°, 2.3°\}$ and $\{0.023°, 0.033°\}$ with the FIM method given by Figs. 6, 7, and 8. The FIM results show that the detector network improves the source localization about two order of magnitudes, while the Bayesian results show that the detector network also plays an important role in eliminating degenerate sky positions. In particular, the inherent multimodal distributions for θ_s and ϕ_s with single detector become unimodal distributions with the detector network. We also find that the estimation errors of $\{q, M_z, d_L, \psi_s, \iota, \phi_{\ell m}\}$ given by the two methods are consistent with each other within one order of magnitude.

V. CONCLUSION

We derive the analytical formulas of the frequency-domain ringdown signals with the harmonic phases, the rotation period of the geocentric detector, and the detector's arm length. The analytical formulas help a lot to reduce the computation time in the FIM analysis. We show the median errors of the parameter estimation and source localization with ringdown signals from binaries with different total masses and different redshifts. We find that for binaries with the total mass $M \geq 10^5\ M_\odot$, space-based GW detectors can effectively estimate parameters and localize sources with the ringdown signal. For the ringdown frequencies $0.5f^* \leq f \leq 5f^*$, we find that the transfer function dramatically improves the parameter estimation and source localization. Thus the transfer function of LISA, Taiji, and TianQin can improve their source localization for binaries with the redshifted total masses $1.7 \times 10^5\ M_\odot \leq M_z \leq 1.7 \times 10^6\ M_\odot$, $2 \times 10^5\ M_\odot \leq M_z \leq 2 \times 10^6\ M_\odot$, and $1.2 \times 10^4\ M_\odot \leq M_z \leq 1.2 \times 10^5\ M_\odot$, respectively. We also find that for BH binaries at the same distance, LISA has larger SNR and better parameter estimation and source localization for the BH binary with $M_z = 6.5 \times 10^6\ M_\odot$, TianQin has larger SNR and better parameter estimation and source localization for the BH binary with $M_z = 3 \times 10^6\ M_\odot$, and LISA-TianQin network has larger SNR and better parameter estimation and source localization for the BH binary with $M_z = 4 \times 10^6\ M_\odot$.

As for the dependence of the parameter estimation and source localization on the sky position, we find that the detector has the best angular resolution for sources along the detector plane, where the relative difference of source location reaches the maximum, but it has the worst angular resolution for sources perpendicular to the detector plane, where the relative difference of source location is the minimum. Except $\{\theta_d, \phi_d\}$, the worst parameter estimation accuracy occurs for sources along the detector plane, where the tensor response is the minimum, and the best parameter estimation accuracy occurs for sources along the two poles, where the tensor response is the maximum. However, the estimation error of the polarization angle ψ_d becomes the worst for sources along the two poles, because of its coupling with ϕ_d. In fact, the difference of the parameter estimation for sources at different locations is within one order of magnitude in most cases.

To check the FIM results, we use Bayesian inference method to analyze two typical binaries. We find that the results of the parameter estimation and source localization given by the two methods are consistent with each other. Thus we expect that in real data analysis, especially in the case of GW detector network, the results of the parameter estimation and source localization given by Bayesian analysis are close to the median errors given by Figs. 6, 7, and 8 within one order of magnitude in most cases.

The network of space-based GW detectors not only improves the sky localization accuracy by two or even three orders of magnitude compared with individual detector, but also avoids the reflected sky position, and it is sensitive to GWs from almost all directions. Thus, to reach the scientific goals efficiently for GW observations, the combined network is extremely important for not only ground-based GW detectors, but also space-based GW detectors. We provide a useful approach to understanding parameter estimation with ringdown signals in space-based GW detectors, which is important to quickly understand the range of possibilities in these detectors. The results are helpful for exploring the scientific potential of space-based GW detectors.

APPENDIX A: ANALYTICAL FORMULAS

In this paper, we use the following formulas:

$$
I_a(\omega_{\ell m}, \tau_{\ell m}, \phi_{\ell m}) = \int_0^{+\infty} e^{-\frac{t}{\tau_{\ell m}}} \cos(\omega_{\ell m} t - \phi_{\ell m}) e^{-i\omega t} dt = \frac{I_{a1} \cos\phi_{\ell m} - I_{a2}\tau_{\ell m}\omega_{\ell m} \sin\phi_{\ell m}}{I_{a3}} \tau_{\ell m},
$$
$$
I_{a1} = (1 + i\omega\tau_{\ell m})[1 + 2i\omega\tau_{\ell m} - \tau_{\ell m}^2(\omega^2 - \omega_{\ell m}^2)],
$$
$$
I_{a2} = \tau_{\ell m}^2(\omega^2 - \omega_{\ell m}^2) - 1 - 2i\omega\tau_{\ell m},
$$
$$
I_{a3} = [\tau_{\ell m}(\omega - \omega_{\ell m}) - i]^2[\tau_{\ell m}(\omega + \omega_{\ell m}) - i]^2, \tag{A1}
$$

$$
I_b(\phi_d, \omega_{\ell m}, \tau_{\ell m}, \phi_{\ell m}) = \int_0^{+\infty} \sin[2(\phi_d - \omega_{tq}t)] e^{-\frac{t}{\tau_{\ell m}}} \cos(\omega_{\ell m} t - \phi_{\ell m}) e^{-i\omega t} dt
$$
$$
= \frac{I_{b1} \cos\phi_{\ell m} - I_{b2}\tau_{\ell m}\omega_{\ell m} \sin\phi_{\ell m}}{I_{b3}} \tau_{\ell m},
$$
$$
I_{b1} = 2\tau_{\ell m}\omega_{tq}[\tau_{\ell m}^2(\omega^2 + \omega_{\ell m}^2 - 4\omega_{tq}^2) - 2i\omega\tau_{\ell m} - 1]\cos 2\phi_d
$$
$$
\quad - (1 + i\omega\tau_{\ell m})[\tau_{\ell m}^2(\omega^2 - \omega_{\ell m}^2 - 4\omega_{tq}^2) - 2i\omega\tau_{\ell m} - 1]\sin(2\phi_d),
$$
$$
I_{b2} = [\tau_{\ell m}^2(\omega^2 - \omega_{\ell m}^2 + 4\omega_{tq}^2) - 2i\omega\tau_{\ell m} - 1]\sin(2\phi_d) + 4\tau_{\ell m}\omega_{tq}(1 + i\omega\tau_{\ell m})\cos 2\phi_d,
$$
$$
I_{b3} = [\tau_{\ell m}(\omega - \omega_{\ell m} - 2\omega_{tq}) - i][\tau_{\ell m}(\omega + \omega_{\ell m} - 2\omega_{tq}) - i]
$$
$$
\quad \times [\tau_{\ell m}(\omega - \omega_{\ell m} + 2\omega_{tq}) - i][\tau_{\ell m}(\omega + \omega_{\ell m} + 2\omega_{tq}) - i], \tag{A2}
$$

$$
\int_0^{+\infty} -e^{-\frac{t}{\tau_{\ell m}}} \sin(\omega_{\ell m} t - \phi_{\ell m}) e^{-i\omega t} dt = I_a\left(\omega_{\ell m}, \tau_{\ell m}, \phi_{\ell m} - \frac{\pi}{2}\right),
$$
$$
\int_0^{+\infty} \cos[2(\phi_d - \omega_{tq}t)] e^{-\frac{t}{\tau_{\ell m}}} \cos(\omega_{\ell m} t - \phi_{\ell m}) e^{-i\omega t} dt = I_b\left(\phi_d + \frac{\pi}{4}, \omega_{\ell m}, \tau_{\ell m}, \phi_{\ell m}\right),
$$
$$
\int_0^{+\infty} -\sin[2(\phi_d - \omega_{tq}t)] e^{-\frac{t}{\tau_{\ell m}}} \sin(\omega_{\ell m} t - \phi_{\ell m}) e^{-i\omega t} dt = I_b\left(\phi_d, \omega_{\ell m}, \tau_{\ell m}, \phi_{\ell m} - \frac{\pi}{2}\right),
$$
$$
\int_0^{+\infty} -\cos[2(\phi_d - \omega_{tq}t)] e^{-\frac{t}{\tau_{\ell m}}} \sin(\omega_{\ell m} t - \phi_{\ell m}) e^{-i\omega t} dt = I_b\left(\phi_d + \frac{\pi}{4}, \omega_{\ell m}, \tau_{\ell m}, \phi_{\ell m} - \frac{\pi}{2}\right),
$$
$$
\int_0^L (e^{2\pi i f[-2L+(1-\mu)\lambda]} + e^{2\pi i f[-L+\lambda-\mu(L-\lambda)]})d\lambda = 2L\mathcal{T}(f, \mu). \tag{A3}
$$

Here $\omega = 2\pi f$.

APPENDIX B: THE COORDINATE TRANSFORMATION

In this section, we give the coordinate transformation formulas from the heliocentric coordinate $\{\hat{i}, \hat{j}, \hat{k}\}$ to the detector coordinate $\{\hat{x}, \hat{y}, \hat{z}\}$. The Euler rotation matrices are

$$
R_x(\theta) = \begin{bmatrix} 1 & 0 & 0 \\ 0 & \cos\theta & -\sin\theta \\ 0 & \sin\theta & \cos\theta \end{bmatrix}, \qquad R_y(\theta) = \begin{bmatrix} \cos\theta & 0 & \sin\theta \\ 0 & 1 & 0 \\ -\sin\theta & 0 & \cos\theta \end{bmatrix}, \qquad R_z(\theta) = \begin{bmatrix} \cos\theta & -\sin\theta & 0 \\ \sin\theta & \cos\theta & 0 \\ 0 & 0 & 1 \end{bmatrix}. \tag{B1}
$$

GW coordinate basis vectors in the heliocentric coordinate are given by

$$\{\hat{m}, \hat{n}, \hat{o}\} = \{\hat{i}, \hat{j}, \hat{k}\} \times R_z(\phi_s - \pi)R_y(\pi - \theta_s)R_z(\psi_s)$$

$$= \begin{bmatrix} \cos\theta_s \cos\phi_s \cos\psi_s + \sin\phi_s \sin\psi_s & \sin\phi_s \cos\psi_s - \cos\theta_s \cos\phi_s \sin\psi_s & -\sin\theta_s \cos\phi_s \\ \cos\theta_s \sin\phi_s \cos\psi_s - \cos\phi_s \sin\psi_s & -\cos\phi_s \cos\psi_s - \cos\theta_s \sin\phi_s \sin\psi_s & -\sin\theta_s \sin\phi_s \\ -\sin\theta_s \cos\psi_s & \sin\theta_s \sin\psi_s & -\cos\theta_s \end{bmatrix}, \quad \text{(B2)}$$

where (θ_s, ϕ_s) are the source location, and ψ_s is the polarization angle.

For TianQin, the detector coordinate basis vectors are

$$\{\hat{x}, \hat{y}, \hat{z}\} = \{\hat{i}, \hat{j}, \hat{k}\} \times R_z\left(\phi_{tq} - \frac{\pi}{2}\right)R_x(-\theta_{tq}), \quad \text{(B3)}$$
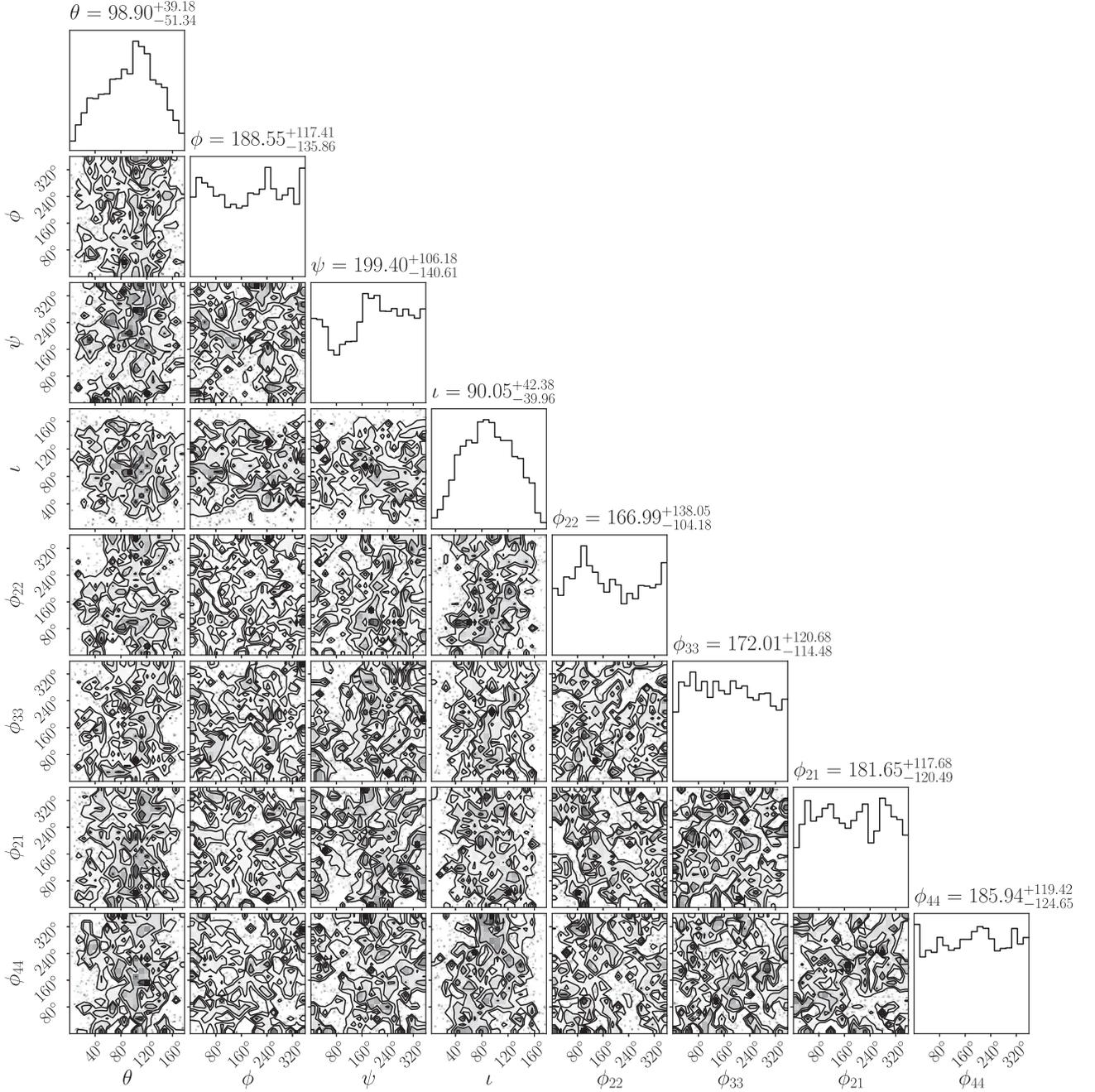

FIG. 18.   The parameter distribution of simulated sources.

where $(\theta_{tq}, \phi_{tq}) = (94.7°, 120.5°)$, and $\omega_{tq} = 2\pi/T_{tq} = 1.99 \times 10^{-5}$ Hz is the rotation frequency of TianQin. For LISA, the detector coordinate basis vectors are

$$\{\hat{x}, \hat{y}, \hat{z}\} = \{\hat{i}, \hat{j}, \hat{k}\} \times R_z(\omega_e t) R_y\left(-\frac{\pi}{3}\right) R_z(-\omega_{lisa}t), \quad (B4)$$

where $\omega_e = \omega_{lisa} = 1.99 \times 10^{-7}$ Hz is the rotation frequency of the Earth and LISA around the Sun. Thus the source parameters in the detector coordinate are

$$\theta_d = \arccos(-\hat{o} \cdot \hat{z}), \qquad \phi_d = 2\arctan\left(\frac{-\hat{o} \cdot \hat{y}}{\sin\theta_d - \hat{o} \cdot \hat{x}}\right),$$

$$\psi_d = 2\arctan\left(\frac{\hat{n} \cdot \hat{z}}{\sin\theta_d - \hat{m} \cdot \hat{z}}\right). \quad (B5)$$

APPENDIX C: SIMULATED SOURCES

For each binary with the same total mass and redshift, we use Monte Carlo simulation to generate 1000 sources. In this Appendix, we show the distribution of the parameters for the simulated sources in Fig. 18.

[1] B. P. Abbott et al. (LIGO Scientific and Virgo Collaborations), Observation of Gravitational Waves from a Binary Black Hole Merger, Phys. Rev. Lett. **116**, 061102 (2016).
[2] B. P. Abbott et al. (LIGO Scientific and Virgo Collaborations), GW151226: Observation of Gravitational Waves from a 22-Solar-Mass Binary Black Hole Coalescence, Phys. Rev. Lett. **116**, 241103 (2016).
[3] B. P. Abbott et al. (LIGO Scientific and Virgo Collaborations), GW150914: The Advanced LIGO Detectors in the Era of First Discoveries, Phys. Rev. Lett. **116**, 131103 (2016).
[4] B. P. Abbott et al. (LIGO Scientific and Virgo Collaborations), GW170104: Observation of a 50-Solar-Mass Binary Black Hole Coalescence at Redshift 0.2, Phys. Rev. Lett. **118**, 221101 (2017); Erratum, Phys. Rev. Lett. **121**, 129901 (2018).
[5] B. P. Abbott et al. (LIGO Scientific and Virgo Collaborations), GW170814: A Three-Detector Observation of Gravitational Waves from a Binary Black Hole Coalescence, Phys. Rev. Lett. **119**, 141101 (2017).
[6] B. P. Abbott et al. (LIGO Scientific and Virgo Collaborations), GW170817: Observation of Gravitational Waves from a Binary Neutron Star Inspiral, Phys. Rev. Lett. **119**, 161101 (2017).
[7] B. P. Abbott et al. (LIGO Scientific and Virgo Collaborations), GW170608: Observation of a 19-solar-mass binary black hole coalescence, Astrophys. J. Lett. **851**, L35 (2017).
[8] B. P. Abbott et al. (LIGO Scientific and Virgo Collaborations), GWTC-1: A Gravitational-Wave Transient Catalog of Compact Binary Mergers Observed by LIGO and Virgo during the First and Second Observing Runs, Phys. Rev. X **9**, 031040 (2019).
[9] R. Abbott et al. (LIGO Scientific and Virgo Collaborations), GW190521: A Binary Black Hole Merger with a Total Mass of 150 $M_\odot$, Phys. Rev. Lett. **125**, 101102 (2020).
[10] R. Abbott et al. (LIGO Scientific and Virgo Collaborations), GW190814: Gravitational waves from the coalescence of a 23 solar mass black hole with a 2.6 solar mass compact object, Astrophys. J. Lett. **896**, L44 (2020).
[11] R. Abbott et al. (LIGO Scientific and Virgo Collaborations), GW190412: Observation of a binary-black-hole coalescence with asymmetric masses, Phys. Rev. D **102**, 043015 (2020).
[12] B. P. Abbott et al. (LIGO Scientific and Virgo Collaborations), GW190425: Observation of a compact binary coalescence with total mass ∼3.4 $M_\odot$, Astrophys. J. Lett. **892**, L3 (2020).
[13] R. Abbott et al. (LIGO Scientific and Virgo Collaborations), GWTC-2: Compact Binary Coalescences Observed by LIGO and Virgo During the First Half of the Third Observing Run, Phys. Rev. X **11**, 021053 (2021).
[14] G. M. Harry (LIGO Scientific Collaboration), Advanced LIGO: The next generation of gravitational wave detectors, Classical Quantum Gravity **27**, 084006 (2010).
[15] J. Aasi et al. (LIGO Scientific Collaboration), Advanced LIGO, Classical Quantum Gravity **32**, 074001 (2015).
[16] F. Acernese et al. (Virgo Collaboration), Advanced Virgo: A second-generation interferometric gravitational wave detector, Classical Quantum Gravity **32**, 024001 (2015).
[17] K. Somiya (KAGRA Collaboration), Detector configuration of KAGRA: The Japanese cryogenic gravitational-wave detector, Classical Quantum Gravity **29**, 124007 (2012).
[18] Y. Aso, Y. Michimura, K. Somiya, M. Ando, O. Miyakawa, T. Sekiguchi, D. Tatsumi, and H. Yamamoto (KAGRA Collaboration), Interferometer design of the KAGRA gravitational wave detector, Phys. Rev. D **88**, 043007 (2013).
[19] K. Danzmann, LISA: An ESA cornerstone mission for a gravitational wave observatory, Classical Quantum Gravity **14**, 1399 (1997).
[20] P. Amaro-Seoane et al. (LISA Collaboration), Laser interferometer space antenna, arXiv:1702.00786.
[21] J. Luo et al. (TianQin Collaboration), TianQin: A spaceborne gravitational wave detector, Classical Quantum Gravity **33**, 035010 (2016).
[22] W.-R. Hu and Y.-L. Wu, The Taiji program in space for gravitational wave physics and the nature of gravity, Natl. Sci. Rev. **4**, 685 (2017).

[23] S. Kawamura *et al.*, The Japanese space gravitational wave antenna: DECIGO, Classical Quantum Gravity **28,** 094011 (2011).

[24] A. G. Riess, S. Casertano, W. Yuan, L. M. Macri, and D. Scolnic, Large magellanic cloud cepheid standards provide a 1% foundation for the determination of the Hubble constant and stronger evidence for physics beyond ΛCDM, Astrophys. J. **876,** 85 (2019).

[25] B. F. Schutz, Determining the Hubble constant from gravitational wave observations, Nature (London) **323,** 310 (1986).

[26] D. E. Holz and S. A. Hughes, Using gravitational-wave standard sirens, Astrophys. J. **629,** 15 (2005).

[27] M. Peterseim, O. Jennrich, and K. Danzmann, Accuracy of parameter estimation of gravitational waves with LISA, Classical Quantum Gravity **13,** A279 (1996).

[28] M. Peterseim, O. Jennrich, K. Danzmann, and B. F. Schutz, Angular resolution of LISA, Classical Quantum Gravity **14,** 1507 (1997).

[29] C. Cutler, Angular resolution of the LISA gravitational wave detector, Phys. Rev. D **57,** 7089 (1998).

[30] C. Cutler and A. Vecchio, LISA's angular resolution for monochromatic sources, AIP Conf. Proc. **456,** 95 (1998).

[31] T. A. Moore and R. W. Hellings, The angular resolution of space based gravitational wave detectors, AIP Conf. Proc. **523,** 255 (2000).

[32] L. Barack and C. Cutler, LISA capture sources: Approximate waveforms, signal-to-noise ratios, and parameter estimation accuracy, Phys. Rev. D **69,** 082005 (2004).

[33] A. Blaut, Accuracy of estimation of parameters with LISA, Phys. Rev. D **83,** 083006 (2011).

[34] M. Vallisneri, Use and abuse of the Fisher information matrix in the assessment of gravitational-wave parameter-estimation prospects, Phys. Rev. D **77,** 042001 (2008).

[35] L. Wen and Y. Chen, Geometrical expression for the angular resolution of a network of gravitational-wave detectors, Phys. Rev. D **81,** 082001 (2010).

[36] B. P. Abbott *et al.* (KAGRA, LIGO Scientific and Virgo Collaborations), Prospects for observing and localizing gravitational-wave transients with Advanced LIGO, Advanced Virgo and KAGRA, Living Rev. Relativity **21,** 3 (2018).

[37] K. Grover, S. Fairhurst, B. F. Farr, I. Mandel, C. Rodriguez, T. Sidery, and A. Vecchio, Comparison of gravitational wave detector network sky localization approximations, Phys. Rev. D **89,** 042004 (2014).

[38] C. P. L. Berry *et al.*, Parameter estimation for binary neutron-star coalescences with realistic noise during the Advanced LIGO era, Astrophys. J. **804,** 114 (2015).

[39] L. P. Singer and L. R. Price, Rapid Bayesian position reconstruction for gravitational-wave transients, Phys. Rev. D **93,** 024013 (2016).

[40] B. Bécsy, P. Raffai, N. J. Cornish, R. Essick, J. Kanner, E. Katsavounidis, T. B. Littenberg, M. Millhouse, and S. Vitale, Parameter estimation for gravitational-wave bursts with the BayesWave pipeline, Astrophys. J. **839,** 15 (2017).

[41] W. Zhao and L. Wen, Localization accuracy of compact binary coalescences detected by the third-generation gravitational-wave detectors and implication for cosmology, Phys. Rev. D **97,** 064031 (2018).

[42] C. Mills, V. Tiwari, and S. Fairhurst, Localization of binary neutron star mergers with second and third generation gravitational-wave detectors, Phys. Rev. D **97,** 104064 (2018).

[43] S. Fairhurst, Localization of transient gravitational wave sources: Beyond triangulation, Classical Quantum Gravity **35,** 105002 (2018).

[44] Y. Fujii, T. Adams, F. Marion, and R. Flaminio, Fast localization of coalescing binaries with a heterogeneous network of advanced gravitational wave detectors, Astropart. Phys. **113,** 1 (2019).

[45] W.-H. Ruan, C. Liu, Z.-K. Guo, Y.-L. Wu, and R.-G. Cai, The LISA-Taiji network: Precision localization of massive black hole binaries, Research **2021,** 6014164 (2021).

[46] W.-H. Ruan, C. Liu, Z.-K. Guo, Y.-L. Wu, and R.-G. Cai, The LISA-Taiji network, Nat. Astron. **4,** 108 (2020).

[47] W.-F. Feng, H.-T. Wang, X.-C. Hu, Y.-M. Hu, and Y. Wang, Preliminary study on parameter estimation accuracy of supermassive black hole binary inspirals for TianQin, Phys. Rev. D **99,** 123002 (2019).

[48] G. Wang, W.-T. Ni, W.-B. Han, S.-C. Yang, and X.-Y. Zhong, Numerical simulation of sky localization for LISA-TAIJI joint observation, Phys. Rev. D **102,** 024089 (2020).

[49] S.-J. Huang, Y.-M. Hu, V. Korol, P.-C. Li, Z.-C. Liang, Y. Lu, H.-T. Wang, S. Yu, and J. Mei, Science with the TianQin Observatory: Preliminary results on Galactic double white dwarf binaries, Phys. Rev. D **102,** 063021 (2020).

[50] C. Zhang, Y. Gong, H. Liu, B. Wang, and C. Zhang, Sky localization of space-based gravitational wave detectors, Phys. Rev. D **103,** 103013 (2021).

[51] C. Zhang, Y. Gong, B. Wang, and C. Zhang, Accuracy of parameter estimations with a spaceborne gravitational wave observatory, Phys. Rev. D **103,** 104066 (2021).

[52] K. J. Shuman and N. J. Cornish, Massive black hole binaries and where to find them with dual detector networks, arXiv:2105.02943.

[53] A. Mangiagli, A. Klein, M. Bonetti, M. L. Katz, A. Sesana, M. Volonteri, M. Colpi, S. Marsat, and S. Babak, On the inspiral of coalescing massive black hole binaries with LISA in the era of Multi-Messenger Astrophysics, Phys. Rev. D **102,** 084056 (2020).

[54] E. Barausse and A. Buonanno, An improved effective-one-body Hamiltonian for spinning black-hole binaries, Phys. Rev. D **81,** 084024 (2010).

[55] Y. Pan, A. Buonanno, R. Fujita, E. Racine, and H. Tagoshi, Post-Newtonian factorized multipolar waveforms for spinning, non-precessing black-hole binaries, Phys. Rev. D **83,** 064003 (2011); Erratum, Phys. Rev. D **87,** 109901 (2013).

[56] I. Kamaretsos, M. Hannam, S. Husa, and B. S. Sathyaprakash, Black-hole hair loss: Learning about binary progenitors from ringdown signals, Phys. Rev. D **85,** 024018 (2012).

[57] I. Kamaretsos, M. Hannam, and B. Sathyaprakash, Is Black-Hole Ringdown a Memory of its Progenitor?, Phys. Rev. Lett. **109,** 141102 (2012).

[58] L. London, D. Shoemaker, and J. Healy, Modeling ringdown: Beyond the fundamental quasinormal modes, Phys. Rev. D **90,** 124032 (2014); Erratum, Phys. Rev. D **94,** 069902 (2016).

[59] V. Baibhav, E. Berti, V. Cardoso, and G. Khanna, Black hole spectroscopy: Systematic errors and ringdown energy estimates, Phys. Rev. D **97,** 044048 (2018).

[60] V. Baibhav and E. Berti, Multimode black hole spectroscopy, Phys. Rev. D **99,** 024005 (2019).

[61] E. Payne, C. Talbot, and E. Thrane, Higher order gravitational-wave modes with likelihood reweighting, Phys. Rev. D **100,** 123017 (2019).

[62] A. Buonanno, G. B. Cook, and F. Pretorius, Inspiral, merger and ring-down of equal-mass black-hole binaries, Phys. Rev. D **75,** 124018 (2007).

[63] E. Berti, V. Cardoso, J. A. Gonzalez, U. Sperhake, M. Hannam, S. Husa, and B. Bruegmann, Inspiral, merger and ringdown of unequal mass black hole binaries: A multipolar analysis, Phys. Rev. D **76,** 064034 (2007).

[64] K. Chatziioannou et al., On the properties of the massive binary black hole merger GW170729, Phys. Rev. D **100,** 104015 (2019).

[65] K. G. Arun, B. R. Iyer, B. S. Sathyaprakash, and S. Sinha, Higher harmonics increase LISA's mass reach for supermassive black holes, Phys. Rev. D **75,** 124002 (2007).

[66] K. G. Arun, B. R. Iyer, B. S. Sathyaprakash, S. Sinha, and C. Van Den Broeck, Higher signal harmonics, LISA's angular resolution and dark energy, Phys. Rev. D **76,** 104016 (2007); Erratum, Phys. Rev. D**76,** 129903 (2007).

[67] M. Trias and A. M. Sintes, LISA observations of supermassive black holes: Parameter estimation using full post-Newtonian inspiral waveforms, Phys. Rev. D **77,** 024030 (2008).

[68] E. K. Porter and N. J. Cornish, The effect of higher harmonic corrections on the detection of massive black hole binaries with LISA, Phys. Rev. D **78,** 064005 (2008).

[69] E. E. Flanagan and S. A. Hughes, Measuring gravitational waves from binary black hole coalescences: 1. Signal-to-noise for inspiral, merger, and ringdown, Phys. Rev. D **57,** 4535 (1998).

[70] K. J. Rhook and J. S. B. Wyithe, Realistic event rates for detection of supermassive black hole coalescence by LISA, Mon. Not. R. Astron. Soc. **361,** 1145 (2005).

[71] E. Berti, V. Cardoso, and C. M. Will, On gravitational-wave spectroscopy of massive black holes with the space interferometer LISA, Phys. Rev. D **73,** 064030 (2006).

[72] C. Shi, J. Bao, H. Wang, J.-d. Zhang, Y. Hu, A. Sesana, E. Barausse, J. Mei, and J. Luo, Science with the TianQin observatory: Preliminary results on testing the no-hair theorem with ringdown signals, Phys. Rev. D **100,** 044036 (2019).

[73] V. Baibhav, E. Berti, and V. Cardoso, LISA parameter estimation and source localization with higher harmonics of the ringdown, Phys. Rev. D **101,** 084053 (2020).

[74] E. K. Porter and N. J. Cornish, Fisher versus Bayes: A comparison of parameter estimation techniques for massive black hole binaries to high redshifts with eLISA, Phys. Rev. D **91,** 104001 (2015).

[75] N. J. Cornish and K. Shuman, Black hole hunting with LISA, Phys. Rev. D **101,** 124008 (2020).

[76] S. Marsat, J. G. Baker, and T. Dal Canton, Exploring the Bayesian parameter estimation of binary black holes with LISA, Phys. Rev. D **103,** 083011 (2021).

[77] M. L. Katz, S. Marsat, A. J. K. Chua, S. Babak, and S. L. Larson, GPU-accelerated massive black hole binary parameter estimation with LISA, Phys. Rev. D **102,** 023033 (2020).

[78] J. Crowder and N. J. Cornish, LISA source confusion, Phys. Rev. D **70,** 082004 (2004).

[79] R.-M. Memmesheimer, A. Gopakumar, and G. Schaefer, Third post-Newtonian accurate generalized quasi-Keplerian parametrization for compact binaries in eccentric orbits, Phys. Rev. D **70,** 104011 (2004).

[80] C. Konigsdorffer and A. Gopakumar, Post-Newtonian accurate parametric solution to the dynamics of spinning compact binaries in eccentric orbits: The Leading order spin-orbit interaction, Phys. Rev. D **71,** 024039 (2005).

[81] E. Cuoco, G. Cella, and G. M. Guidi, Whitening of nonstationary noise from gravitational wave detectors, Classical Quantum Gravity **21,** S801 (2004).

[82] N. J. Cornish and T. B. Littenberg, BayesWave: Bayesian inference for gravitational wave bursts and instrument glitches, Classical Quantum Gravity **32,** 135012 (2015).

[83] J. Carre and E. K. Porter, The effect of data gaps on LISA galactic binary parameter estimation, arXiv:1010.1641.

[84] M. Tinto and J. W. Armstrong, Cancellation of laser noise in an unequal-arm interferometer detector of gravitational radiation, Phys. Rev. D **59,** 102003 (1999).

[85] J. W. Armstrong, F. B. Estabrook, and M. Tinto, Time-delay interferometry for space-based gravitational wave searches, Astrophys. J. **527,** 814 (1999).

[86] K. Dey, N. Karnesis, A. Toubiana, E. Barausse, N. Korsakova, Q. Baghi, and S. Basak, Effect of data gaps on the detectability and parameter estimation of massive black hole binaries with LISA, Phys. Rev. D **104,** 044035 (2021).

[87] E. Barausse and L. Rezzolla, Predicting the direction of the final spin from the coalescence of two black holes, Astrophys. J. Lett. **704,** L40 (2009).

[88] G. L. Israel et al., Rxj0806.3+1527: A double degenerate binary with the shortest known orbital period (321s), Astron. Astrophys. **386,** L13 (2002).

[89] S. C. C. Barros, T. R. Marsh, P. Groot, G. Nelemans, G. Ramsay, G. Roelofs, D. Steeghs, and J. Wilms, Geometrical constraints upon the unipolar model of V407 Vul and RX J0806.3 + 1527, Mon. Not. R. Astron. Soc. **357,** 1306 (2005).

[90] G. H. A. Roelofs, A. Rau, T. R. Marsh, D. Steeghs, P. J. Groot, and G. Nelemans, Spectroscopic evidence for a 5.4-minute orbital period in HM cancri, Astrophys. J. Lett. **711,** L138 (2010).

[91] P. Esposito, G. L. Israel, S. Dall'Osso, and S. Covino, Swift X-ray and ultraviolet observations of the shortest orbital period double-degenerate system RX J0806.3 + 1527 (HM Cnc), Astron. Astrophys. **561,** A117 (2014).

[92] T. Kupfer, V. Korol, S. Shah, G. Nelemans, T. R. Marsh, G. Ramsay, P. J. Groot, D. T. H. Steeghs, and E. M. Rossi, LISA verification binaries with updated distances from Gaia Data Release 2, Mon. Not. R. Astron. Soc. **480,** 302 (2018).

[93] T. Robson, N. J. Cornish, and C. Liu, The construction and use of LISA sensitivity curves, Classical Quantum Gravity **36,** 105011 (2019).

[94] D. Liang, Y. Gong, A. J. Weinstein, C. Zhang, and C. Zhang, Frequency response of space-based interferometric gravitational-wave detectors, Phys. Rev. D **99**, 104027 (2019).

[95] C. Zhang, Q. Gao, Y. Gong, D. Liang, A. J. Weinstein, and C. Zhang, Frequency response of time-delay interferometry for space-based gravitational wave antenna, Phys. Rev. D **100**, 064033 (2019).

[96] C. Zhang, Q. Gao, Y. Gong, B. Wang, A. J. Weinstein, and C. Zhang, Full analytical formulas for frequency response of space-based gravitational wave detectors, Phys. Rev. D **101**, 124027 (2020).

[97] J. S. Speagle, dynesty: A dynamic nested sampling package for estimating Bayesian posteriors and evidences, Mon. Not. R. Astron. Soc. **493**, 3132 (2020).

[98] J. Skilling, Bayesian Inference and Maximum Entropy Methods in Science and Engineering, in *Proceedings of the 24th International Workshop on Bayesian Inference and Maximum Entropy Methods in Science and Engineering*, edited by R. Fischer, R. Preuss, and U. V. Toussaint, American Institute of Physics Conference Series Vol. 735 (American Institute of Physics Publishing, New York, 2004), pp. 395–405.

[99] J. Skilling, Nested sampling for general Bayesian computation, Bayesian Anal. **1**, 833 (2006).